LBL--18699

DE85 007078

INCLUSIVE PRODUCTION OF STRANGE AND VECTOR MESONS IN e^+e^- ANNIHILATION AT 29 GeV

Heidi Marie Schellman
Ph.D. Thesis

Lawrence Berkeley Laboratory
University of California
Berkeley, California 94720

November 1984

This work was supported by the Director, Office of Energy Research, Office of High Energy and Nuclear Physics, Division of High Energy Physics of the U.S. Department of Energy under Contract Number DE-AC03-76SF00098.

Inclusive Production of Strange and Vector Mesons in e^+e^- Annihilation at 29 GeV

Heidi Marie Schellman

ABSTRACT

The Mark II detector is used to measure the inclusive production rates for K^0, $K^\pm$, ρ^0, K^{*0} and $K^{*\pm}$ in a sample of 59,489 hadronic events produced in e^+e^- annihilation at 29 GeV. The inclusive rates for ρ^0 and $K^{*0}+\overline{K}^{*0}$ production for momenta greater than 1 GeV/c are found to be $0.44 \pm 0.04 \pm 0.06$ per event and $0.42 \pm 0.05 \pm 0.08$ per event respectively. The rate for $K^{*\pm}$ production for momenta greater than 2 GeV/c is found to be $0.26 \pm 0.05 \pm 0.06$ per event. The rate for $K^0 + \overline{K}^0$ production over the full momentum range is found to be $1.27 \pm 0.03 \pm 0.15$ per event.

The differential production rates for K^0, ρ^0 and $K^{*\pm}$ are, in addition, determined as a function of the particle energy. The inclusive rate for $K^\pm$ is also measured for $K^\pm$ momenta less than 900 MeV/c and is found to be $1.31 \pm 0.09 \pm 0.19$ times the $K^0+\overline{K}^0$ rate in the same momentum region. These production rates are used to determine the particle content of hadronic events at 29 GeV and are compared to the rates predicted by theoretical models of parton fragmentation.

Table of Contents

Chapter 1: Introduction

One of the features of high multiplicity hadronic events, regardless of the underlying process, is the dominance of pions among the final state particles. For example, in e^+e^- annihilation at 29 GeV, the TPC collaboration [1] finds a $\pi^\pm$ to $K^\pm$ ratio of 8 to 1. At a very naive level, this is quite surprising. The energy scale for the event as a whole is 29 GeV; compared to this scale the difference between pion and kaon masses is negligible and one would expect nearly equal production rates. A more sophisticated approach would take vector meson decays into account. One would expect 3 vector mesons for every pseudo-scalar meson due to spin statistics. Vector mesons decays enhance the number of pions and have little effect on the number of kaons. The inclusion of vector mesons would raise the expected pion to kaon ratio to 2.5 to 1. This ratio is still far less than the observed ratio. One can keep introducing more nonets of mesons, such as the tensor and scalars or one can introduce an intermediate mass scale of order 1-2 GeV. Such an intermediate scale would induce the suppression of higher mass mesons observed in the data.

Two classes of hadronization models introduce such a mass scale. The string models [2] explain hadronization as a quantum mechanical tunnelling process in a 1-dimensional color field. This color field has an energy density of order 1 GeV/fermi. Typical hadron sizes of 1 fermi introduce a mass scale of order 1

GeV. In this model the color string is assumed to possess no angular momentum. This constrains the mesons produced from the string to the 0^- and 1^- spin-parity assignements allowed for an s-wave $q\bar{q}$ state.

Cluster models [3, 4, 5] use leading-log perturbative QCD to produce a shower of partons. At a mass scale of order 1-2 GeV, the partons are combined to form color singlet clusters. These clusters then decay into mesons and baryons by phase space alone. Figure 1.1 illustrates a typical parton shower with the subsequent cluster decays. In this model, any spin-parity is possible for the mesons produced. Higher mass nonets are only suppressed by mass effects.

Both classes of models thus introduce an intermediate mass scale which can suppress kaon production. A notable feature of both models is that the intermediate mass scale determines the properties of hadronization. This implies that the details of hadronization should be insensitive to the event energy and thus that studies of hadronization at 29 GeV may be directly applicable at higher energies.

In this dissertation I present measurements of strange and vector meson production rates in e^+e^- annihilation. As these mesons have masses between 0.5 and 1 GeV they provide a sensitive test of these hadronization models. Chapters 2 through 4 are devoted to a description of the Mark II detector and to determination of the production rates. In Chapter 5 the suppression factors for strange and vector mesons in hadronization are estimated in a model independent fashion. Chapter 6 is devoted to the comparison of the data with specific models.

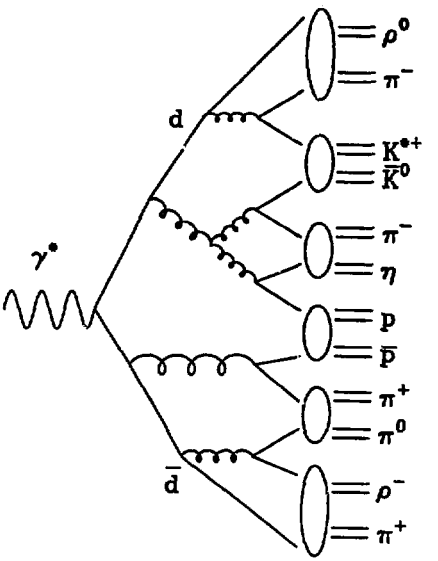

Figure 1.1: Cluster model hadronization of an $e^+e^- \rightarrow d\bar{d}$ event. The straight lines represent quarks, the looping lines represent gluons and the ellipses represent the low mass cluster decays.

Chapter 2: The Mark II at PEP

2.1 PEP

The data discussed in this dissertation were collected with the Mark II detector during 4 years of running at the PEP (Positron Electron Project) ring located at SLAC (Stanford Linear Accelerator Center). PEP is a large positron-electron storage ring 2.2 km in circumference with 6 interaction regions. Three bunches each of positrons and electrons circulate, colliding every 2.4 μsec at each interaction region. The beams interact in a region with an effective rms width 480μm in the horizontal (x) direction, 60μm in the vertical (y) direction and 1.5 cm along the beam (z) direction.

2.2 DETECTOR

The Mark II [6] is a general purpose spectrometer designed for the study of e^+e^- annihilations in the center of mass frame. In the central two thirds of the solid angle there are drift chambers for momentum determination, a Time of Flight system for identifying slow moving hadrons, a liquid argon electromagnetic calorimeter for electron and photon identification and 4 layers of steel and proportional tubes for muon identification. In addition, at smaller polar angles there are lead proportional chamber endcaps and a Small Angle Tagger system used for identifying small angle electrons and for luminosity determination.

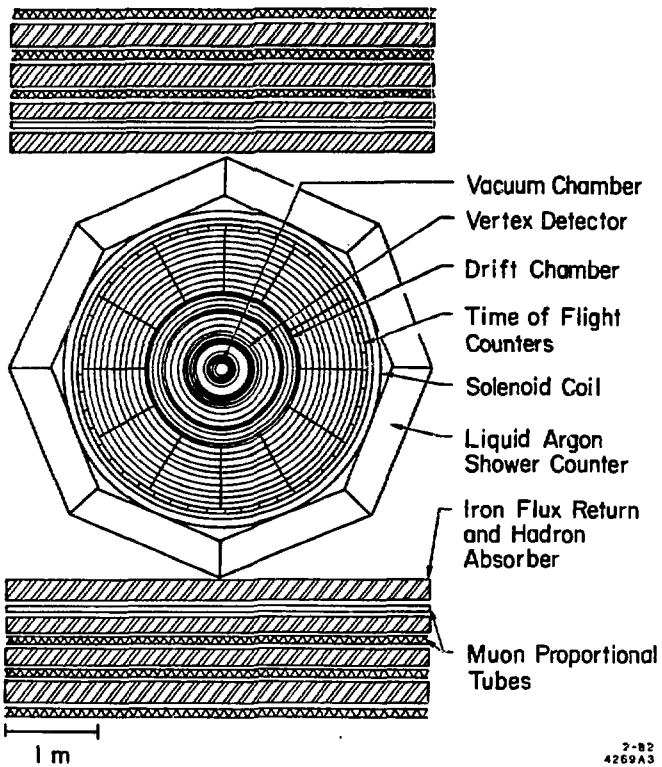

Figure 2.1: Mark II detector at PEP – view along the beam axis.

The Mark II has had several different configurations during its long lifespan. Originally installed at SPEAR, it ran at center of mass energies between 3 and 7.4 GeV from 1978 to 1979. It was then moved to the PEP ring where it collected data at 29 GeV from 1980 to 1984. The detector configuration that is described here is that which existed for the bulk of the PEP running. The analysis discussed in this dissertation relies almost entirely on the drift chambers and time of flight system. Only these systems will be described. Fig 2.1 shows the detector in the final configuration which existed for most of the PEP running.

Magnet The Mark II magnet is a conventional room temperature solenoid with the field direction parallel to the beam or z axis. The magnet coil is outside the central drift chambers and Time of Flight system and just inside the liquid argon calorimeter. It consists of two layers of water cooled aluminum conductor. The original field was 4.64 kG but a short circuit occurred between the inner and outer coils in early 1982. For the bulk of the data described here only the outer coil was powered; the resulting field was 2.3 kG. The field shape was mapped with a Hall probe before the coil was installed at SPEAR and the absolute normalization of the field was monitored during data taking by a nuclear magnetic resonance probe near the beam pipe.

Vertex Chamber The vertex chamber, or VC, [7] is a high precision cylindrical drift chamber installed after the first year of PEP running. It consists of two narrow bands of sense wires, one of 4 layers beginning at a radius of 10.4 cm with respect to the beams and one of 3 layers beginning at a radius of 30.5 cm. Sense wires have a spacing of $\sim$ 1 cm and can detect the ionization of a passing charged track with spatial resolution of 95 μm. Both the vertex chamber and the main

drift chamber use a gas mixture of 50% ethane and 50% argon at atmospheric pressure.

To minimize multiple scattering errors the beam pipe consists of 1.4 mm of beryllium with 50μm of titanium on the inner side for shielding from synchrotron radiation and 50 μm of mylar and 20 μm of aluminum on the outer side to form the inner wall of the vertex chamber. Table 2.1 gives details of the materials in the beam pipe and other detector components.

Main Drift Chamber The main drift chamber(DC) [8] was a part of the original SPEAR Mark II and continued in service until 1984. It consists of 16 equally spaced concentric layers of drift wires lying between radii of 41 and 145 cm. To provide z and dip angle information, the layers alternate between angles of 0, +3 and -3 degrees with respect to the beam axis. The inner 6 layers have a sense wire spacing of 1.8 cm and the outer 10 have a spacing of 3.6 cm. The rms spatial resolution is 220 μm per wire.

At 2.3 kG magnetic field the combined information from the main and vertex chambers allow determination of the track parameters with rms resolutions:

$$\left(\frac{\delta p_\perp}{p_\perp}\right)^2 = (0.025)^2 + (0.01 p_\perp)^2$$

$$\delta x^2, \delta y^2 = (115/p_\perp)^2 + (85)^2 \mu\mathrm{m}^2$$

$$\delta \tan(\frac{\pi}{2} - \theta)^2 = (3.1/p_\perp)^2 + (3.9)^2 mr^2$$

$$\delta \phi^2 = (1.0/p_\perp)^2 + (0.4)^2 mr^2$$

where the first error is the multiple scattering error, the second is the measurement error and p is in GeV/c. These values are derived from the error matrices of track fits. The combined drift and vertex chambers allow charged particle tracking over $\sim$ 80% of the solid angle.

	material	Average Radius(cm)	Thickness (cm)	Radiation Lengths
Vertex Chamber				
Beam pipe	Ti	7.7	0.005	—
	Be	"	0.140	0.006
	Mylar	"	0.005	—
	Al	"	0.002	—
Gas	Ar-Ethane	7.8-35.0	27.1	0.002
Outer skin	Al	35.	0.178	0.020
Main Drift Chamber				
Inner skin	Lexan	37.3	0.32	0.009
Gas	Ar-ethane	37.4-150.3	113.0	0.009
Outer skin	Al	150.7	0.64	0.071
Time of Flight				
	Pilot F	151.1-153.6	2.5	0.064
Magnet				
	Al	159-173	14.0	1.40
Calorimeter				
	Pb-Ar	~ 180	41.0	14.0

Table 2.1: Detector Materials

The efficiency of the drift chamber for charged tracks with $p_\perp$ greater than 100 MeV/c and $\cos\theta$ well within the solid angle has been estimated [9, 10] to be 95-97%. These values apply when the chambers were operating well. For a large portion the data sample used in this dissertation, the main drift chamber operated at reduced voltages. In the worst case, the tracking efficiency

was reduced to 90% of the optimal value. The effects of reduced chamber voltage are discussed in some detail in Chapter 3.

Time of Flight The Time of Flight (or TOF) system consists of 48 scintillation counters at a radius of 1.51 m. Each scintillator is read out at both ends by phototubes. The rms timing resolution is around 350 psec allowing the unique identification of π, K and protons up to momenta of $\sim$ 1 GeV/c and the separation of protons from π and K up to $\sim$ 2 GeV/c over 75% of the solid angle. Where information from both ends of the counter is available and only one track enters a scintillator, the z position of the track in the scintillator can be measured with an rms resolution of 8 cm. These counters are $\sim$ 99% efficient for charged tracks. Confusion due to multiple hits and interactions by neutral tracks in the scintillator reduce the fraction of tracks which produce good time of flight information to around 65%.

Beam Position Monitor The high precision of the drift chambers in x and y allows stringent cuts on the positions of tracks. Movements in the interaction point for different machine configurations are often much larger than the precision of the tracking. To monitor these movements we use an online beam position monitor and offline calculations of mean beam positions.

A beam position monitor (BPM) is located at each end of the detector just inside the final quadrupole magnet 4.9 m from the interaction point. Each BPM consists of 4 buttons arranged at 0, 90, 180 and 270 degrees around the beam pipe. The voltages induced on the buttons by the passage of electrons are measured for 96 beam crossings every 4 minutes during data taking. This provides a record of relative beam motions during a run which can later be

compared with average beam positions determined from drift chamber tracks. The relative measurements of beam positions within a run are accurate to 20μm but the absolute measurement over many runs is prone to drift.

2.3 TRIGGER

The Mark II has a two level trigger. The fast Primary trigger system determines whether a possible event has occurred for each beam crossing. If an event looks interesting, the Secondary trigger is used to determine if the event information should be read out to the VAX-11/780.

The Primary trigger for charged events requires hits in several drift chamber layers and in at least 1 time of flight counter. There is also a neutral energy trigger requiring a minimum amount of energy in the liquid argon system and a SAT trigger based on the SAT scintillators used for low angle bhabhas. The primary trigger takes only 1 μsec to make a decision. If there is a primary trigger, data taking is stopped for 30μsec while the secondary trigger makes a decision.

The secondary trigger system uses fast electronics to look for patterns of drift chamber hits and TOF information consistent with a charged track. A trigger requires either 2 or more such tracks or 1 GeV of energy in at least 2 of the 8 liquid argon calorimeters or the 2 end caps. If the secondary trigger is satisfied the data are read out to the VAX-11/780 and written to tape. The primary trigger rate is around 1 kHz, resulting in a 3% dead time due to the 30 μsec secondary trigger delay. The secondary trigger rate is typically 3 Hz. Such triggers are almost all due to beam interactions with residual gas in the beam pipe or to electronic pick-up in the detector. At the peak luminosity of $3 \times 10^{31}/\text{cm}^2 - \text{sec}$ the rate for hadronic events is only 0.01 Hz. This trigger is

> 99% efficient for hadronic events which passed standard event quality cuts. These cuts require a minimum of 5 charged tracks and 7.25 GeV in charged energy.

Data is logged in 'runs' which correspond to a machine fill or to the amount of data which fills a tape. Runs typically last from 1 to 3 hours and contain 5,000–20,000 triggers.

2.4 EVENT RECONSTRUCTION

Event reconstruction is done on an IBM 3081 and an IBM 3033 mainframe computer at SLAC. The raw data written to tape is first searched for charged tracks in the drift and vertex chambers. Candidate tracks require at least 7 total hits with at least 4 hits in stereo layers. This requirement provides an over-constrained fit to the 5 parameters of the track helix. An additional parameter allows the track to bend slightly at the interface between the vertex and drift chambers to account for multiple scattering.

After all charged tracks have been found, an event vertex is found by constraining the tracks to a common origin in space. Tracks which lie far from the origin or which contribute a very large χ^2 are not included. Tracks are then traced outwards into the other detector systems and associated with information in those components. The calorimeters are also searched for energy deposition from neutral particles.

The position of the interaction point is determined on a run-by-run basis by calculating the average x, y and z for the ensemble of tracks in that run.

After full event reconstruction is done, the data are filtered with very loose cuts to remove events due to beam-gas interactions and low energy photon-photon interactions. For example, in the filtering program, hadronic events are

defined as those with at least one fourth of the total energy in charged and neutral tracks, at least one eighth of the total energy in charged tracks and at least 5 charged tracks. As these cuts are looser than the definition of a hadronic event used in this analysis, they have no effect on the final hadron sample. The remaining events in the filtered sample consist of $e^+e^- \to e^+e^-$, $\mu^+\mu^-$, $\tau^+\tau^-$, hadrons and residual background.

After filtering the data are used to refine the constants used in drift chamber reconstruction. The filtered data are then retracked with these refined constants.

Chapter 3: Inclusives I. ρ^0 and K^{*0}

In this chapter I describe the measurement of ρ^0 and K^{*0} production rates. This measurement involves several factors; the selection of hadronic events, the ρ^0 and K^{*0} signals, estimates of the detection efficiencies and a normalization. These will each be treated in some detail as the methods used are applicable to all of the analyses presented in this dissertation.

3.1 HADRONIC EVENTS

A typical hadronic event at PEP energies has a detected charged multiplicity of 11 and 50% of the beam energy appears as charged tracks. Figure 3.1 shows such a typical event.

Backgrounds Several other processes can produce events which mimic hadronic events.

a) The process $e^+e^- \to \tau\bar{\tau}$ produces events with 2-6 charged tracks which can carry a sizeable fraction of the center of mass energy.

b) Two photon processes, illustrated in Figure 3.2, produce hadronic events with low effective beam energy and large net momentum along the beam axis.

c) Interactions of the beams with residual gas in the vacuum pipe produce low energy events with large net momentum along the beam axis. These events will be evenly distributed along the z axis.

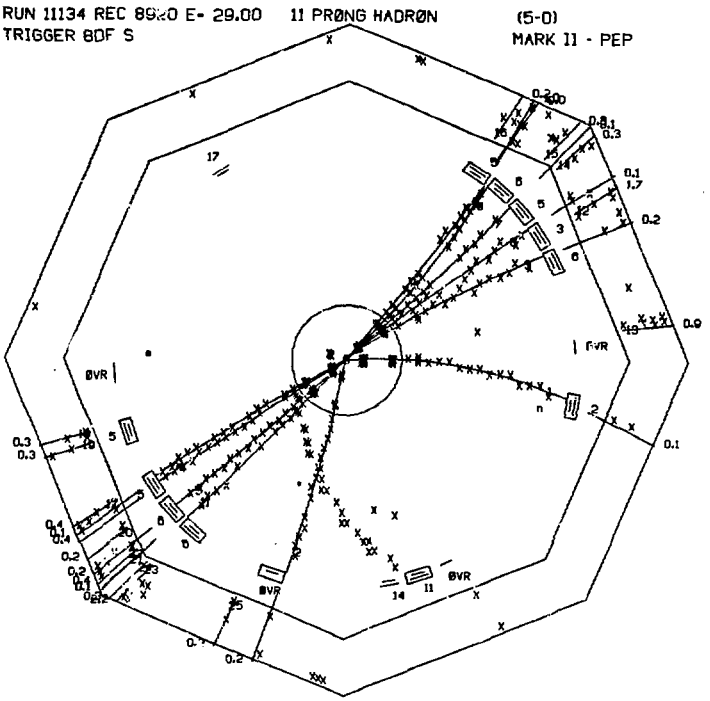

Figure 3.1: Typical event viewed along the z axis

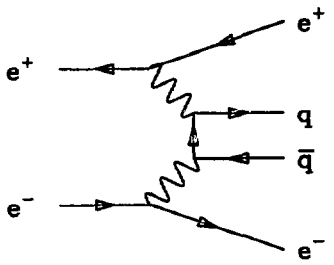

Figure 3.2: Feynman diagram for two-photon process

Cuts In order to reduce these backgrounds we have chosen reasonably stringent cuts to define the hadronic event sample. Charged tracks are first subjected to quality cuts:

a) $p < E_{beam}$ – poor tracking can result in tracks with very large momenta.

b) $p_{xy} \equiv \sqrt{p_x^2 + p_y^2} \geq 0.1$ GeV/c

c) $|\cos\theta| \leq 0.85$ – (within drift chamber acceptance)

d) $|z_{dca}| \leq 10$ cm– (dca means distance of closest approach to the beam interaction point)

e) $|r_{dca}| \leq 2$ cm if $p \geq 1$ GeV/c or $|r_{dca}| \cdot p \leq 2$ cm GeV/c if $p < 1$ GeV/c – As tracks with p less than 1 GeV/c will have a larger rms r due to multiple scattering, the cut must be widened.

A hadronic event is defined as one with:

a) at least 5 'good' charged tracks whose total energy of is greater than $\frac{1}{4}$ of the center-of-mass energy.

b) The sphericity axis determined from the charged tracks is required to lie within $|\cos\theta| < .65$ – this assures that most of the event energy is in fact contained in the detector.

c) The event vertex is required to lie within 10 cm of the average beam interaction point in z and 2 cm in r.

In the full data sample of 220 pb^{-1}, a total of 59,498 hadronic events are detected.

The hadronic event cross section was studied in detail by J. Patrick and V. Lüth [9] before the installation of the vertex chamber. The cuts used in their analysis were in general less stringent than those used here and did not include the sphericity axis cut. They estimated contributions of:

a) $\tau\bar{\tau} = 2.5 \pm 0.5\%$ of the 'hadron' sample. I estimate that this is lowered to $2.0 \pm 1.0\%$.

b) 2-photon and beam gas $= 1.5 \pm 0.8\%$. The effects of tighter cuts are offset by increases in beam current for data samples taken after the Patrick analysis was done. Higher beam currents lead to larger beam gas contributions. I estimate a contribution of $1.5 \pm 1.0\%$.

The hadronic event sample thus has at most $3.5 \pm 1.5\%$ contamination from other processes.

3.2 ρ^0 AND K^{*0}

ρ^0 and K^{*0} decay strongly to $\pi\pi$ and $K\pi$ respectively.† Tracks from the charged decay modes resemble other charged tracks in an event. This creates a large combinatorial background which prevents the identification of ρ^0 and K^{*0} on an event by event basis. The ρ^0 and K^{*0} production rates are measured from fits to the $\pi\pi$ and $K\pi$ mass spectra. The data sample used in this analysis is the full hadronic event sample at PEP with an integrated luminosity of 220 pb^{-1}.

3.3 TRACK PAIR SELECTION

Tracks which are to be used in the mass plots are subjected to slightly more stringent cuts than those used in event selection:

a) $p_{xy} \geq 0.2$ GeV/c – this cut assures that the track momenta are well measured.

b) $|\cos\theta| \leq 0.75$

c) $|z_{dca}| \leq 5.0$ cm

d) $|r_{dca}| \leq 0.5$ cm if $p \geq 1$ GeV/c and $|r_{dca}| \cdot p \leq 0.5$ cm GeV/c if $p \leq 1$ GeV/c – A tight cut on r_{dca} eliminates most tracks from K^0 and Λ decays as well as most mis-measured tracks.

These cuts are deliberately kept loose to avoid biasing the center of mass decay angle distribution. As vector particles could be polarized a cross section measurement is most model independent if made over the full range of decay angles. No attempt at particle identification is made and each pair of tracks is considered as

† K^{*0} should be taken to mean both K^{*0} and $\overline{K}^{*0}$ unless otherwise stated. The same applies to K^0.

$\pi\pi$, Kπ and πK. The pair invariant masses are then accumulated for unlike-sign pairs. Figures 3.3a and b show the invariant mass distributions.

3.4 FITS

The $m_{\pi\pi}$ and $m_{K\pi}$ distributions are fit simultaneously. Both distributions contain contributions from

$$K_S \to \pi^+\pi^-, \qquad \rho^0 \to \pi^+\pi^-, \qquad K^{*0} \to K^+\pi^-, \qquad \text{and} \qquad \omega \to \pi^+\pi^-\pi^0.$$

Most of the $K_S \to \pi^+\pi^-$ are removed by the 5 mm impact parameter cut but contributions from ω, ρ^0 and K^{*0} decays are comparable and must be accounted for correctly.

Decay shapes The expected shapes of the various resonance contributions are found by Monte Carlo methods (described in the following sections). Events are generated and are used to produce simulated hadronic event raw data. Pairs of reconstructed tracks which pass all of the cuts and which are identified as the decay products of a resonance are histogrammed with $\pi\pi$, Kπ and πK hypotheses, just like the data. (The identification of produced and detected tracks is done by comparing the drift chamber information for a detected track with the information associated with a produced track. The produced track which contributes the majority of hits to a detected track is assumed to have produced that detected track.) The $\pi^+\pi^-$ pairs from ω decay in the Monte Carlo are weighted by the true decay matrix element to produce the correct $m_{\pi\pi}$ contribution. This procedure yields the resonance shapes and the shapes of the distributions resulting from π-K confusion. As the track parameters used are the reconstructed quantities, the resonance shapes reflect the mass resolution of the detector.

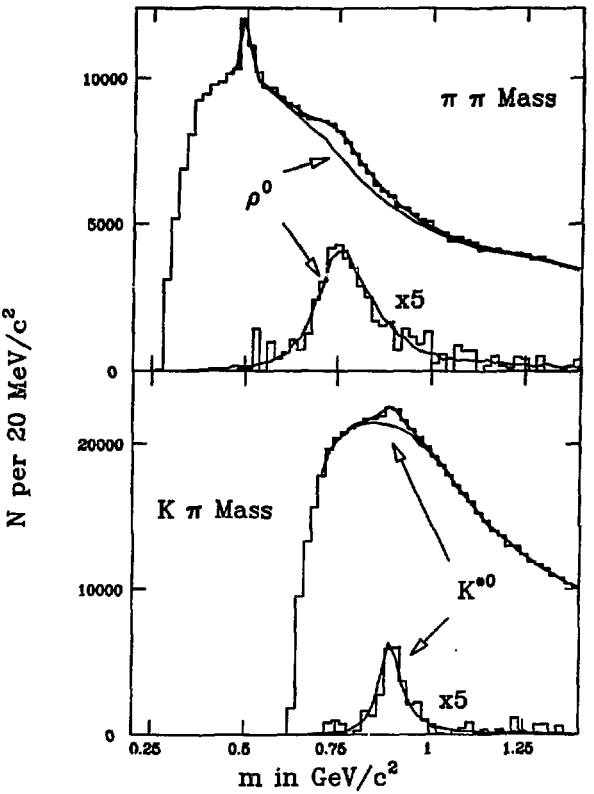

Figure 3.3: Fits to $\pi^+\pi^-$ and $K^+\pi^-$ mass spectra – The curves show the background function and the background plus the signal. The background subtracted signal is shown as well with $\times 5$ magnification.

The mass distributions are then fit to the sums of the resonance contributions and quartic polynomials. Pairs with $0.440 < m_{\pi\pi} < 1.400$ GeV/c^2 or $0.700 < m_{K\pi} < 1.400$ GeV/c^2 are included in the fit. This fit, in principle, involves 12 free parameters: the numbers of ρ^0, K^{*0}, ω and K^0 and separate quartics for the $\pi^+\pi^-$ and $K^+\pi^-$ mass distributions.† In practice, the ω contribution is not well determined and is fixed to be equal to the ρ^0 population. This assumption is the major source of systematic error in the K^* cross section and is discussed in more detail later. Figures 3.3 and 3.4 show the ρ and K^* fits. The fits yield 10480 ± 1040 ρ^0 and 6384 ± 690 charged decays of K^{*0} and $\bar{K}^{*0}$. The χ^2/dof is 66.0/72 with a $\rho^0 - K^{*0}$ correlation coefficient derived from the error matrix of 0.029.

In order to transform the raw numbers of ρ^0 and K^{*0} into production rates, the reconstruction efficiency must be estimated. The next few sections describe our method of efficiency determination in some detail.

3.5 Efficiencies

We use a standard hadronic event Monte Carlo model to generate events and then use a simulation program to generate the appropriate detector response to the events. These simulated raw data are then subjected to the same pattern recognition programs as the real data. Both the produced event quantities and the detected event quantities are stored.

An event model need only mimic the kinematics of events to provide an estimate of efficiencies. This requirement is fulfilled by QCDJET, [11] an

† The two fit functions are normalized to the data for both mass hypotheses. This imposes two constraints on the parameters and reduces the number of free parameters from 14.

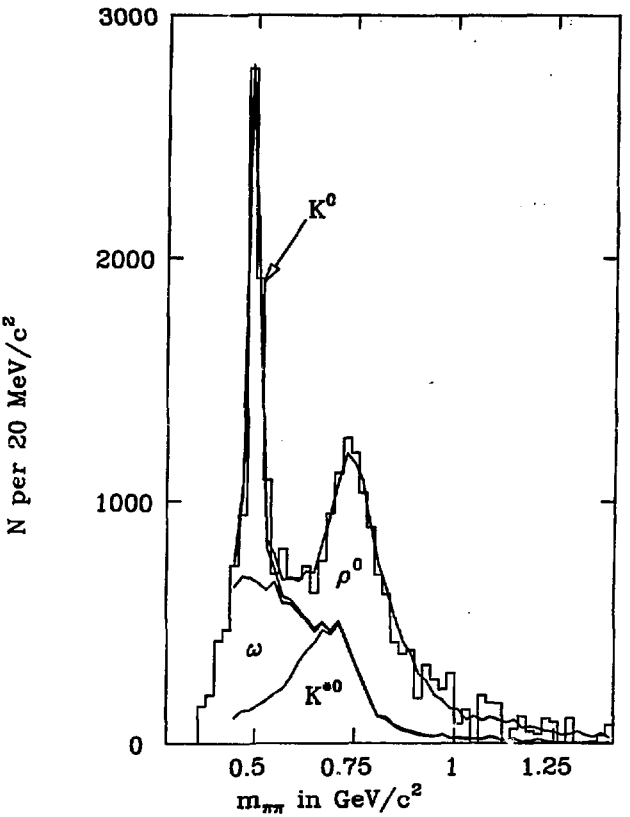

Figure 3.4: Fit to $\pi^+\pi^-$ mass spectrum – The quartic background has been subtracted to display the contribution of each resonance.

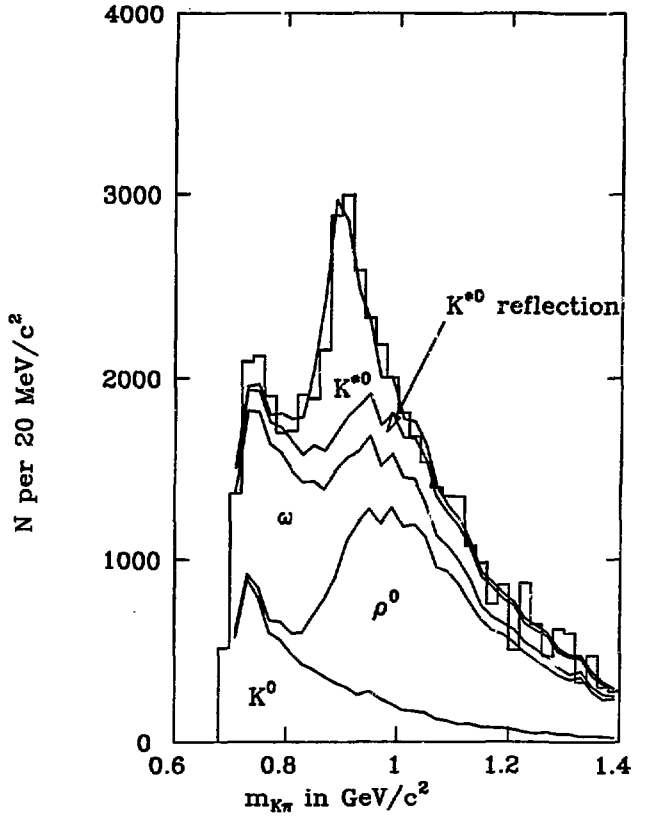

Figure 3.4: (continued) Fits to $K^+\pi^-$ mass spectrum – The quartic background has been subtracted to display the contribution of each resonance.

e^+e^- hadronic Monte Carlo which includes QCD diagrams up to second order in the strong coupling constant, α_s, and uses a Field-Feynman [12] fragmentation scheme to produce final state particles from quarks and gluons. The version used by the Mark II collaboration is BQCD, a variant of standard QCDJET which includes baryon production.

At 29 GeV each initial quark in an event will produce a jet of particles. To first order there will be two back-to-back jets. QCD corrections produce events with gluons and hence 3 or 4 jets. These corrections raise the total hadronic event cross section by 5−10% and produce events of different shapes than those with just two quark jets. QCDJET can be tuned to match the cross section and event shapes measured in the data quite well.

Once the initial quarks and gluons have been generated, the Field-Feynman method is used to create the final state particles. Each parton is fragmented separately. The algorithm takes the initial u, d, s, c or b quark and creates a quark-antiquark pair from the vacuum; the anti-quark is joined with the initial quark to form a meson while the algorithm starts over with the left-over quark and creates a new pair (Fig. 3.5).

Parameters of the model determine the probability that a pair created from the vacuum has flavor u, d or s, the spin of the meson, the sharing of energy between the meson and leftover quark and the $p_\perp$ of the meson. When most of the initial quark energy has been used, the algorithm is used on the initial anti-quark in the event until most of the initial anti-quark energy has been used. The left-over quark and anti-quark are then joined to form a final meson.

The sharing of energy between the meson and the left-over quark is described by a splitting or fragmentation function. This function is generally

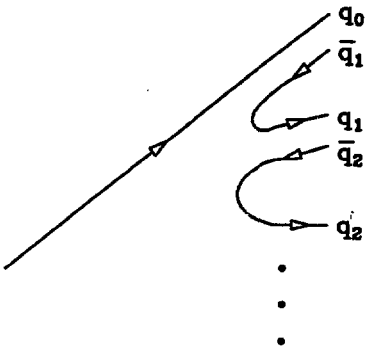

Figure 3.5: Field Feynman fragmentation algorithm

parameterized with the light-cone variable:

$$z = \frac{E_i^m + p_{\parallel i}^m}{E_{i-1}^q + p_{\parallel i-1}^q}$$

where $(E_i^m + p_{\parallel i}^m)$ is the energy + parallel momentum of the meson and E_{i-1}^q is the energy of the parent quark. z can be interpreted as the fraction of the energy of a quark which goes into the meson while $1 - z$ is the fraction which remains with the left-over quark. Kinematics indicate that a light meson will share its energy evenly with the light left-over quark while a heavy meson such as D or B will acquire most of the initial heavy quark energy, leaving little for the left-over quark. The splitting functions used in this analysis are:

$$f(z) = (1-z)^r \qquad r = 0.7 \text{ for u, d and s quarks}$$

$$f(z) = \frac{1}{z}\frac{1}{(1-1/z-\frac{\epsilon}{1-z})^2} \qquad \epsilon = 0.3 \text{ for c quarks and .03 for b quarks}$$

Gluons are fragmented by splitting them into a quark-antiquark pair and then fragmenting the quark and anti-quark.

This method of fragmentation has several flaws:

1) It does not take meson masses into account except by not producing them when there is not enough energy.
2) It is not Lorentz invariant and does not conserve energy and momentum step by step. The final meson momenta must be adjusted in order to assure momentum conservation.
3) It assumes that each step is independent of any other and thus cannot include interference or Bose-Einstein effects.

Physics predictions of this model should therefore be used with care. Despite this, the model does do a good job of reproducing the gross characteristics of the data. This is all that is needed for efficiency determination. Table 3.1 summarizes the parameters of the model.

3.6 Radiative Corrections

e^+e^- cross sections are usually quoted as if only the first order QED diagram contributed. As real data include contributions from higher order QED diagrams a correction must be made. In addition, any Monte Carlo used for efficiency calculations should include higher order QED diagrams to mimic the data. The total cross section for hadronic event production of order α^3 is [13, 14]:

$$\sigma(s) = \sigma_0(s)\Big[1+\delta+\frac{2\alpha}{\pi}\int_{k_{min}}^{E}\Big(1-\frac{k}{E}+\frac{k^2}{2E}\Big)\frac{\sigma_0(4E(E-k))}{\sigma_0(4E^2)}\frac{dk}{k}\Big]$$

QCDJET parameters	
quark flavors	u,d,s,c,b
QCD diagrams	qq, qqG, qqGG, qqqq
Gluon spin	1
Gauge boson (γ or Z^0)	γ only
Λ_{QCD} in GeV	0.30
strange fraction in fragmentation	0.20
rms $p_\perp$ for quarks	0.30
light quark vector fraction	0.58
r in light quark splitting function: $f(z) = 1 - a + a(r+1)(1-z)^r$	0.70
a in light quark splitting function	1.00
Cutoff on (1-thrust) for 3 jet events	0.05
Cutoff on acoplanarity for 4 jet events	0.05
rms $p_\perp$ for quarks from gluons	0.30
ϵ_c in charm splitting function: $f(z) = (1/z)(1 - 1/z - \epsilon/(1-z))^{-2}$	0.30
ϵ_b in beauty splitting function	0.03
charm quark vector fraction	0.75
BQCD parameters	
di-quark fraction in fragmentation	0.10
rms $p_\perp$ for di-quarks	0.36
r in di-quark splitting function: $f(z) = 1 - a + a(r+1)(1-z)^r$	2.00
a in di-quark splitting function	1.00

Table 3.1: Summary of the parameters of the hadronic event production model BQCD used for efficiency calculations in this analysis.

where E is the beam energy, s is $(2E)^2$, σ_0 is the first order cross section and k is the energy of the radiated photon. The integral corresponds to those diagrams with a radiated photon of energy greater than k_{min}. The δ term takes into account higher order diagrams with no detectable final state photon. These consist of vacuum polarization diagrams and those diagrams with photons of energy less than k_{min}. k_{min} is set to 1% of the beam energy; for this value, δ is around -0.23.

In the Monte Carlo the cross section is divided into two parts:

$$\sigma_{no-rad} = \sigma_0(1+\delta)$$

and

$$\sigma_{rad} = k \text{ integral.} \times \sigma_0$$

The raw efficiency for finding a particle in an event is

$$\epsilon_{raw}(x) = \frac{N(x)\text{detected}}{N(x)\text{produced}}$$

where x is any kinematical variable. In order to quote a radiatively corrected cross section an additional efficiency factor of

$$\begin{aligned}\epsilon_{rad}(x) &= \frac{N(x)\text{produced}}{N(x)\text{first order}} = \frac{\sigma(x)}{\sigma_0(x)} \\ &= \frac{N(x)\text{produced}}{N(x)\text{no}-\text{rad}}(1+\delta)\end{aligned}$$

is needed. The effect of this radiative correction is two-fold. First, the $1+\delta$ factor corrects for changes in the total cross section due to the vacuum diagrams and very soft radiation. Second, initial state radiation changes the momentum spectrum of final state particles. Very high momenta are depopulated and the lowest momenta are somewhat over-populated. The radiative correction attempts to reconstruct the true momentum distribution at the nominal beam energy. This

reconstruction is only accurate if the momentum dependence of the cross section is known at all energies or if the correction is small. In the present analysis the mean beam energy after radiation is 27.9 GeV in detected events. The mean correction is thus small.

These efficiencies can be combined to form

$$\epsilon_0(x) = \frac{N(x)\text{detected}}{N(x)\text{no}-\text{rad}}(1+\delta)$$

The radiatively corrected cross section for a process will then be

$$\sigma_0(x) = \frac{N(x)\text{ in data}}{\text{I} \times \epsilon_0(x)}$$

where I is the integrated luminosity for the data sample.

3.7 RATE CALCULATIONS

The production rate per hadronic event for a particle species is:

$$R(x) = \frac{\sigma_p(x)}{\sigma_H} = \frac{\frac{N(x)\text{in data}}{\text{I}\times\epsilon_0(x)}}{\frac{N_H\text{in data}}{\text{I}\times\epsilon_H}} = \frac{N(x)/N_H}{\epsilon_0(x)/\epsilon_H}$$

where N_H is the number of detected hadronic events and ϵ_H is the detection efficiency for hadronic events. In this analysis N_H is corrected for the 2% $\tau^+\tau^-$ background. The efficiencies quoted in this dissertation will be the ratio $\epsilon_0(x)/\epsilon_H$ which can be interpreted as the efficiency for finding a meson in a detected event.

Several sources of systematic error cancel in the rate calculation. The cancellation of the luminosity is obvious but errors due to the hadronic event efficiency and radiative corrections also tend to cancel.

Hadron efficiency The efficiency for detecting a particle species with a charged decay mode is roughly

$$\epsilon \sim (\epsilon_T)^n \times \epsilon_H$$

where ϵ_T is the single charged track efficiency and n is the number of charged tracks into which the particle decays. This is a consequence of the necessity of detecting the hadronic event before any particle in it can be found. To the extent that this approximation is true, the hadronic event efficiency cancels in the rate calculation.

The hadronic event cuts rid the sample of most events with large initial state radiation. The residual effect of radiative corrections is a small adjustment of the momentum spectra, of order 3%.

We estimate a total error of 5% on rate measurements due to uncertainties in the radiative corrections, model dependence of the hadronic event efficiency and background contamination of the hadron sample. These sources of error would exist even with a perfect detector. In the following sections I describe the effects of detector imperfections.

3.8 Detector Simulation

I have described the event generator and radiative corrections. To be useful in understanding our detector performance a Monte Carlo program must also simulate the response of the detector to the produced event.

Once the initial particles in an event have been generated, they are traced outward from their point of origin, as if they were real particles. Where they encounter material, multiple scattering and energy loss are simulated. The program simulates drift chamber hits by first calculating the distance of closest approach of the track to the wires which it passes. A simple polynomial time-distance relation is used to determine a drift time from the distance of closest approach. The drift time is then smeared with a gaussian error. Both the time-distance and error distributions are somewhat simpler than those for a real drift

chamber. Despite these simplifications the simulated data is quite similar to real data taken under optimal conditions.

Checks of the Detector Simulation This simulation was tested for the main drift chamber at SPEAR [15] with data from the decay $\psi' \to \psi \pi^+ \pi^-$ with a subsequent leptonic decay of the ψ. The well defined kinematics of the decays allow the momentum of the fourth track to be reconstructed even if only 3 of the 4 tracks were actually detected. This allowed a precise absolute determination of the tracking efficiency. The Monte Carlo prediction of the efficiency agreed with this absolute number to within 1%. This study shows that the drift chamber simulation performed very well for the main drift chamber with low multiplicity events.

At PEP, events are far more complex than those found at SPEAR. Mean multiplicities for events which pass the hadronic event cuts are around 12 with the tracks concentrated in jets. In addition, many changes have been made to the detector. The major change is the installation of the vertex chamber after the first year of PEP running. The vertex chamber is included in the tracking algorithm and increases the solid angle slightly as fewer hits are needed in the main drift chamber to reconstruct a track. The tracking code was changed substantially to accommodate the vertex chamber. As a result of these changes the tracking procedure is not wholly analogous to the methods used for the SPEAR data.

After several years of running, the main drift chamber began to have problems holding voltage at high beam currents. To allow data taking while the chamber was not running well the voltage on the chamber was lowered below optimal levels with significant reduction of the tracking efficiency. Around 40% of the data sample was collected under these conditions. The addition of 0.7%

oxygen to the drift chamber gas allowed eventual restoration of the drift chamber voltage to optimal levels.

The effects of cuts on r and z for several data and Monte Carlo samples have been studied to gain some understanding of the effects of the PEP environment on the tracking efficiency. The standard event cuts are used to define an event sample. The number of individual tracks per event is then studied as a function of the cuts. As the physics of hadronic events does not change with time, any variation between data samples indicates changes in the detector efficiency or resolution.

Tracks with $p_{xy} > 200$ MeV/c and $|\cos\theta| < .75$ are divided into three samples.

- POOR tracks are all of those with either $r > 1$ cm or $z > 20$ cm. These are mostly tracks which are severely mis-reconstructed.
- GOOD tracks are those with both $r < 5$ mm and $z < 5$ cm. These are almost certainly well-reconstructed.
- SO-SO tracks are those which are in between GOOD and POOR.

The data are divided into 8 samples determined by running conditions. Table 3.2 summarizes the number of tracks per event for each of these samples.

The VC and NEW samples are clearly the best and agree with each other quite well. The Monte Carlo parameters were *chosen* to make it agree with the VC sample for tight cuts.

Fig 3.6 shows the number of tracks passing cuts in r and z as a function of the cut. The good agreement between the MC, VC and NEW samples is essentially independent of the cuts. The BAD sample is clearly less efficient with substantial variation in the relative loss as the cuts are varied. The relative

Sample	events	TOTAL	POOR	SO-SO	GOOD	comment
DC	4140	10.53	1.83	0.58	8.12	no vertex chamber
VC	5152	10.25	1.33	0.67	8.25	vertex chamber
BAD1	11384	10.26	1.71	1.24	7.31	DC voltage low
BAD2	10097	10.25	1.57	1.04	7.64	DC voltage low
RES	11384	10.35	1.42	0.81	8.12	oxygen added
NEW1	11206	10.40	1.40	0.76	8.24	DC wires replaced
NEW2	10873	10.40	1.39	0.73	8.28	"
MC	-	9.93	1.10	0.61	8.22	Monte Carlo
VC/MC		1.03	1.21	1.10	1.00	ratio

Table 3.2: Number of tracks per event for different data samples. The statistical errors on these numbers are less than 0.05.

losses between samples have also been studied as a function of momentum. No momentum dependence is found.

From this I conclude that the Monte Carlo does an excellent job of reproducing the effects of cuts on the VC, RES and NEW data samples. There is a residual 3% discrepancy in the ratio of total to good tracks between the Monte Carlo and VC samples. The discrepancy arises in those tracks which have both bad r and z. This may be due to a larger number of imaginary tracks in the VC sample but is more likely due to an increased probability of seriously mis-tracking real tracks. As either case is possible, I assume that the Monte Carlo efficiency for single tracks is $1.5 \pm 1.5\%$ too high. This correction is to be applied to all charged tracks.

The Monte Carlo indicates that 5% of all produced tracks which fall within the solid angle of the drift chamber have no associated reconstructed

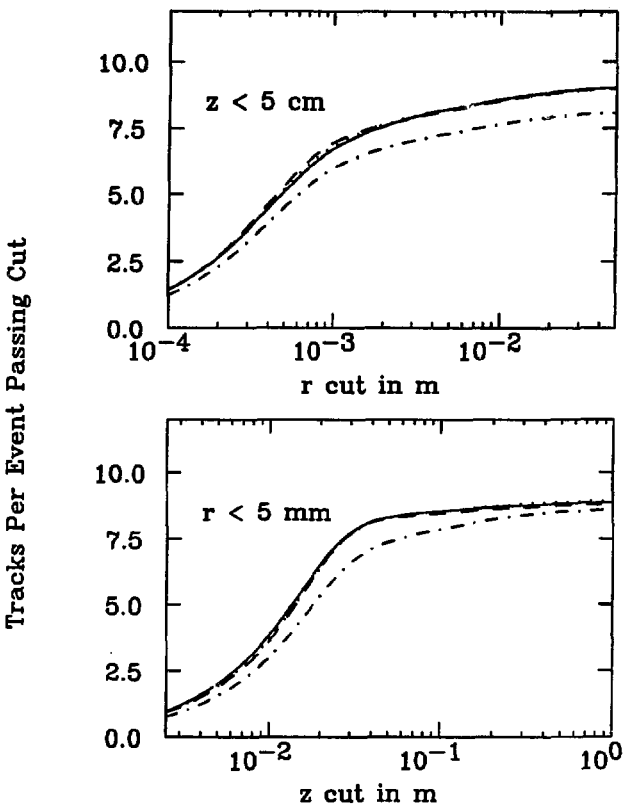

Figure 3.6: Effects of cuts on the number of tracks for the VC (solid), MC (dashed), NEW1 (dotted) and BAD1 (dot-dash) samples. Tracks used in the r cut study are required to pass tight z cuts and vice-versa.

track. This factor may be different in the data. I assign an additional error of 2.5% to the tracking efficiency for this unknown quantity. The total error on the efficiency is thus 3% per track.

The other data samples, DC and BAD are not reproduced well by the Monte Carlo simulation. (The DC sample has no efficiency problems but has a different detector geometry.) They can only be used where it is possible to estimate a correction for the efficiency loss from the data. This is in fact possible for the ρ^0 and K^{*0} measurements where the reconstruction efficiency is closely related to the single track efficiencies.

In summary, we believe that we can measure production rates with a 3% error per track due to the tracking efficiency and a 5% error from the normalization, radiative corrections and model dependence.

3.9 ρ^0 AND K^{*0} EFFICIENCIES

With the efficiency correction procedure understood we can now evaluate the production rates for K^{*0} and ρ^0. As the full data sample, including bad data is used there are two efficiency corrections to make. There is the Monte Carlo efficiency described in the previous sections which includes radiative corrections and a correction for variations in tracking efficiency in the different data samples.

Tracking efficiency We estimate the effects of tracking efficiency by taking the best data sample, (NEW), and comparing the total number of pairs per event passing the cuts for ρ^0 and K^{*0} in that data with the number in the whole sample as a function of pair mass and pair momentum. For pairs with masses near the ρ mass and $p \geq 1$ GeV/c there is a $7 \pm 1\%$ greater loss in the full sample. There is little variation in this correction as a function of momentum. Including the 1.5% per track correction for the difference between the best data and the Monte Carlo, the ρ^0 efficiency for the whole data sample is 90% of that given by the Monte Carlo. The corresponding efficiency factor for K^{*0} is also 90%.

The systematic error in this efficiency due to differences between the Monte Carlo and the best sample is estimated above to be around 3% per track. As there are two tracks involved there is a possible 6% systematic error on the efficiency due to uncertainties in the tracking efficiency.

Geometric and fit efficiencies The Monte Carlo efficiency is calculated from a comparison of the number of ρ^0 and K^{*0} produced in non-radiative events with the number 'detected' in all events passing the hadronic event cuts. The number 'produced' is defined as the number of resonances made in the Monte Carlo which

decay into 2 charged tracks. The neutral decay of the K^{*0} is taken into account by multiplication of the final production rate by $\frac{2}{3}$ and is not included in the quoted efficiencies. There are two possible definitions for 'detected':

a) The numbers of produced ρ^0 and K^{*0} which have both tracks passing all cuts and identified as coming from the resonance. No requirement is made that the tracks actually be properly reconstructed. The statistical error on this efficiency is small. This efficiency will be referred to as ϵ_G where G is for Geometric.

b) The numbers of ρ^0 and K^{*0} detected by the analysis when it is run on a Monte Carlo sample. This efficiency takes into account errors due to the fitting procedure, but has larger statistical errors. This will be referred to as ϵ_F. ϵ_F can be calculated for each momentum bin, but the statistics in some of the bins are too low to provide a good estimate. As a compromise the geometric efficiency is used to estimate the momentum dependence and an overall correction of ϵ_F/ϵ_G averaged over all momenta is made to construct $\epsilon_F(p)$. This $\epsilon_F(p)$ is used for cross section calculations and is summarized in Table 3.3.

Radiative corrections are done as described in the previous sections and the efficiency divided by the hadronic event efficiency to get the probability of finding a ρ^0 or K^{*0} in a detected hadronic event. The rate is then normalized to the number of hadrons.

3.10 Fit Results

With the efficiencies understood the production rates for ρ^0 and $K^{*0}+\bar{K}^{*0}$ can finally be calculated and are given in Table 3.4.

p	$\epsilon_G(p)$	$\epsilon_F(p) = \frac{\epsilon_F}{\epsilon_G}\epsilon_G(p)$
1.0 – 2.0	0.347 ± 0.004	0.381 ± 0.035
2.0 – 3.0	0.422 ± 0.006	0.463 ± 0.042
3.0 – 5.0	0.470 ± 0.006	0.516 ± 0.047
5.0 – 7.0	0.507 ± 0.009	0.557 ± 0.051
7.0 – 10.0	0.519 ± 0.011	0.570 ± 0.052
1.0 – 14.5	0.418 ± 0.003	0.459 ± 0.042

Table 3.3: Radiatively corrected efficiencies for detection of $\rho^0 \to \pi^+\pi^-$ in a detected hadronic event. The corresponding efficiencies for K^{*0} with $p \geq 1$ GeV are $\epsilon_G = 0.402 \pm 0.003$, $\epsilon_F = 0.439 \pm 0.048$. The tracking losses and branching fractions are not included in these values.

	N in fit	Corrected N per event	χ^2/dof
ρ^0	10480 ± 1040	0.435 ± 0.043	66.0/72
$K^{*0} + \overline{K}^{*0}$	6384 ± 690	0.416 ± 0.045	
$\frac{K^{*0}+\overline{K}^{*0}}{\rho^0}$		0.96 ± 0.14	

Table 3.4: Results of Simultaneous Fit to $\pi^+\pi^-$ and $K^+\pi^-$ for $p \geq 1$ GeV/c. The $\rho^0 - K^{*0}$ correlation coefficient is 0.029. The number of K^{*0} from the fit includes only charged decay modes.

There are enough data to determine the ρ^0 cross section for several momentum bins. If it is assumed that the ρ^0 and K^{*0} rates have similar momentum

dependences, the measured ratio of K^{*0} to ρ^0 for the full momentum range can be used as an estimate of the ratio in each momentum bin. The $\pi\pi$ spectrum is then fit alone for the ρ^0 rate as a function of p. The assumption that the K^{*0} and ρ^0 rates have similar momentum dependences is borne out by the $K^{*\pm}$ spectrum measured in Chapter 4. Table 3.5 gives the results of these fits and Fig. 3.7 shows the ρ^0 differential cross section as a function of $x_\rho = E_\rho/E_{\rm beam}$ compared with results from the TASSO [16] and JADE [17] collaborations.

p, GeV/c	N_ρ	χ^2/dof
1.0 - 2.0	2815 ± 960	46.4/42
2.0 - 3.0	2370 ± 470	62.7/42
3.0 - 5.0	2249 ± 415	44.9/42
5.0 - 7.0	1463 ± 281	32.6/42
7.0 - 10.0	1067 ± 240	53.6/42
total		
1.0 - 10.0	9964 ± 865	
x	Corrected number per event	$\frac{1}{\beta\sigma_H}\frac{d\sigma_\rho}{dx}$
0.087-0.148	0.141 ± 0.034	2.60 ± 0.61
0.148-0.214	0.098 ± 0.019	1.56 ± 0.31
0.214-0.349	0.083 ± 0.015	0.63 ± 0.12
0.349-0.485	0.050 ± 0.010	0.38 ± 0.07
0.485-0.692	0.036 ± 0.008	0.18 ± 0.04
total		
0.087-0.692	0.408 ± 0.042	

Table 3.5: ρ^0 Differential Cross Section – statistical errors only.

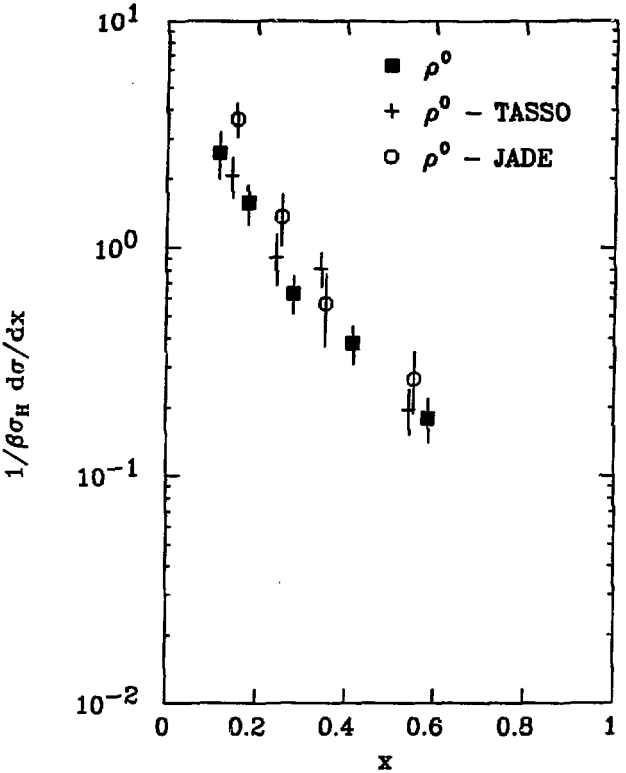

Figure 3.7: Comparison of ρ^0 differential cross section from Mark II, TASSO and JADE – statistical errors only.

$p \geq 2$ GeV/c In order to make later comparisons with $K^{*\pm}$ results the distributions are also fit for $p \geq 2$ GeV/c. The results are summarized in Table 3.6:†

	N in fit	Corrected number per event	ratio	χ^2/dof
ρ^0	6872 ± 840	0.254 ± 0.030		74.1/72
$K^{*0} + \bar{K}^{*0}$	4355 ± 520	0.243 ± 0.029		
K^{*0}/ρ^0			0.95 ± 0.17	

Table 3.6: Results of Simultaneous Fit to $\pi^+\pi^-$ and $K^+\pi^-$ for $p \geq 2$ GeV/c. The $\rho^0 - K^{*0}$ correlation coefficient is 0.058.

3.11 CHECKS

In order to check the fitting procedure the same analysis has been done for like-sign pairs and Monte Carlo where the production is known. This provides

† The difference between the number of ρ^0 found in the simultaneous fits for $p > 1$ GeV/c and $p > 2$ GeV/c is 0.18 ρ^0 per event. This is somewhat higher than the value of 0.141 ± 0.034 found in the fit to the momentum bin from 1 to 2 GeV/c. As the data sample is the same one would expect the difference to be much less than the statistical error. I believe that the difference comes from the contribution of the ρ^0 reflection in the $K\pi$ mass spectrum which affects the simultaneous fits but not the fits to the $\pi\pi$ spectrum alone. The two estimates of the rate from 1 to 2 GeV/c are thus, to some extent, statistically independent.

a check on the errors and indicates any systematic bias in the fitting procedure. The following checks are described below:

- Fit to like-sign pairs,
- Fit to Monte Carlo,
- Fit to Monte Carlo background sample,
- Effects of ω rate,
- Effects of K^{*0} mass, and
- Changes to the fit ranges over which the $\pi\pi$ and $K\pi$ masses are fit.

Like-sign pairs The like-sign distributions for $p \geq 1$ GeV/c are fit in the same fashion as the unlike-sign. The fit yields $-1984 \pm 1823\rho^0$ and $427 \pm 570K^{*0}$ where none are expected. In a similar fit to a Monte Carlo like-sign distribution, the numbers found are $-185 \pm 540\rho^0$ and $852 \pm 365K^{*0}$.

Monte Carlo Two different Monte Carlo samples are fit with the combined Monte Carlo sample used to determine the decay mass shapes. Table 3.7 shows the results. When the results of the two fits are combined it appears that the number of ρ^0 found is $10 \pm 9\%$ high and the number of K^{*0} is $9 \pm 12\%$ too high. Although these differences are hardly significant, they are corrected for by the use of ϵ_F.

To better understand the source of the over-estimate, we study pairs in the Monte Carlo sample which are known to be from background with no signal contributions. This background sample is constructed from all pairs which do not come from the same resonances. Individual tracks which come from a resonance are included only if they are paired with another random track and not their

	found	produced	χ^2/dof
Sample I			
ρ^0	7439 ± 764	6361	75.9/72
K^{*0}	3981 ± 504	3602	
Sample II			
ρ^0	5083 ± 663	4931	54.8/72
K^{*0}	3146 ± 435	2845	

Table 3.7: Results of fit to Monte Carlo for $p \geq 1$ GeV/c

	background	found *minus* produced from Table 3.7	χ^2/dof
Sample I			
ρ^0	1221 ± 690	1078 ± 764	84.3/72
K^{*0}	117 ± 450	379 ± 504	
Sample II			
ρ^0	-116 ± 612	152 ± 663	66.4/72
K^{*0}	248 ± 399	301 ± 435	

Table 3.8: Results of fit to background for $p \geq 1$ GeV/c

partner. Table 3.8 compares the results of the fits to the background with the discrepancy seen in the fits in Table 3.7.

The discrepancy between the produced and fit values seems to be explained by the underlying background. The variation in this background contribution from sample to sample seems large. (ϵ_P corrects for the discrepancy and

$\omega =$	ρ^0	$0.5\rho^0$	$1.5\rho^0$
N_{ρ^0}	10480 ± 1040	9859 ± 990	10858 ± 1075
$N_{K^{*0}}$	6384 ± 690	5700 ± 685	7161 ± 709
$\frac{K^{*0} \to K^+\pi^-}{\rho^0}$	0.609	0.578	0.660
χ^2	66.0	70.7	63.8

Table 3.9: Results of changing N_ω for $p \geq 1$ GeV/c

has a large statistical error ($\sim 10\%$) which will be included in the systematic errors discussed below.)

Effects of ω The above fits assume equal ρ^0 and ω production. As only the $\pi^+\pi^-$ from the ω are visible, the $\pi^+\pi^-$ pair has a lower momentum than the ω itself. As the ω momentum spectrum has not been measured, the Monte Carlo ω and ρ^0 spectra and the *measured* ρ^0 momentum spectrum are used to estimate it. The number of $\pi^+\pi^-$ pairs from ω decay that are put into the fit in a given momentum bin i is:

$$N^i_\omega = \left[\frac{N^i_{\pi^+\pi^-} \text{ from } \omega \text{ in MC}}{N^i_{\pi^+\pi^-} \text{ from } \rho^0 \text{ in MC}}\right](N^i_{\rho^0} \text{ found in fit})$$

The ω contribution calculated above could depend on the momentum spectra of ρ^0 and ω produced in the Monte Carlo. This has been checked for two widely different fragmentation schemes

$$f(z) = (1-z)^2 \text{ and } f(z) = (1-z)^{0.7}$$

which lead to a 3% difference in the number of ρ^0 found.

To study the effects of variations of the ω cross section on the results, we redo the fits fixing the ratio of ω and ρ^0 to 0.5 and 1.5. (See Table 3.9.)

The results for the number of ω left as a free parameter are summarized in Table 3.10.

$\omega =$	ρ^0	free
$\sigma_\omega/\sigma_{\rho^0}$	1.00	1.63 ± 0.43
N_{ρ^0}	10480 ± 1040	11042 ± 1229
$N_{K^{*0}}$	6384 ± 690	7424 ± 1029
$\frac{K^{*0} \to K^+\pi^-}{\rho^0}$	0.609	0.672
χ^2	66.0	63.8

Table 3.10: Results of letting N_ω vary for $p \geq 1$ GeV/c

On the assumption that the ω/ρ^0 ratio has high probability of being in the range 0.5 to 1.5, we estimate contributions to the systematic uncertainty of -5.9% and $+3.6\%$ for the ρ^0, $\pm 10.9\%$ for the K^{*0} and -5.1% and $+8.4\%$ for the ratio of K^{*0} to ρ^0.

<u>K^{*0} Mass</u> The $K\pi$ mass spectra in Figures 3.3 and 3.4 appears to peak at a slightly higher value than the standard K^* mass. The fit, redone with the K^* mass allowed to vary, gives the results summarized in Table 3.11:

The best fit K^{*0} mass seems to be slightly high, although the K_S mass is measured correctly (next chapter) to within 1 MeV/c^2. The cross sections quoted below are based on the fit with the K^{*0} mass fixed to the nominal value.

<u>Effects of fit range</u> The fits have been redone with changes in the $\pi\pi$ and $K\pi$ mass ranges included in the fit. The results are consistent within the statistical errors and are summarized in Table 3.12:

	fixed	free
$m_{K^{*0}}$, GeV/c^2	0.896	$0.905 \pm .004$
N_{ρ^0}	10480 ± 1040	10055 ± 1050
$N_{K^{*0}}$	6384 ± 690	6671 ± 795
$\frac{K^{*0}}{\rho^0}$	.609	.663
χ^2/dof	66.0/72	61.2/71
$\rho^0 - K^{*0}$ correlation	0.025	.451

Table 3.11: Results of letting $m_{K^{*0}}$ vary for $p \geq 1$ GeV/c

$m_{\pi\pi}$(GeV/c^2)	N_ρ	$m_{K\pi}$(GeV/c^2)	N_{K^*}	χ^2/dof
0.440-1.400	10480 ± 1040	0.700-1.400	6384 ± 690	66.0/72
0.440-1.200	11805 ± 1624	0.700-1.200	6207 ± 806	48.4/69
0.440-1.400	10381 ± 1050	0.760-1.400	6668 ± 825	62.9/69
0.400-1.400	10184 ± 1025	0.700-1.400	6172 ± 675	69.0/74

Table 3.12: Effects of fit range

The variations in the fit ranges change N_ρ by -2.9% and $+12.6\%$ and $N_{K^{*0}}$ by $\pm 4.4\%$. The ratio changes by -13% and $+4.5\%$. These changes are consistent with the statistical errors of 10% for ρ^0 and 11% for K^{*0}.

All of these checks combined imply that the fits yield results which are accurate to around 15%. Table 3.13 summarizes the various estimates of the systematic errors. The error on the ratio is reduced as the tracking efficiency and normalization errors cancel.

		ρ^0	K^{*0}	ratio
fit systematics:				
	ω cross section	$^{+3.6}_{-5.9}$%	±10.8%	$^{+5.4}_{-5.1}$%
	error on ϵ_F	± 9%	±12%	±15%
normalization:				
	Tracking efficiency	± 6%	± 6%	cancels
	Model and normalization	± 5%	± 5%	cancels
Total		±13%	±18%	±17%

Table 3.13: Estimate of Systematics

3.12 INCLUSIVE RATES

In summary the rates are $0.435 \pm 0.043 \pm 0.057$ ρ^0 and $0.416 \pm 0.045 \pm 0.075$ K^{*0} and $\overline{K}^{*0}$ per event with $p > 1$ GeV/c. The ratio of $K^{*0} + \overline{K}^{*0}$ to ρ^0 is $0.96 \pm 0.14 \pm 0.17$. In the limit of SU(3) symmetry this ratio would be 2.

Extrapolation to $p < 1$ GeV/c The Monte Carlo indicates that 65% of ρ and 67% of K^{*0} have p greater than 1.0 GeV/c. (The Monte Carlo reproduces the observed ρ^0 spectrum to within the sizeable errors.) This indicates 0.67 ± 0.07 ρ^0 per event and 0.62 ± 0.07 $K^{*0} + \overline{K}^{*0}$ where the errors are statistical only.

Chapter 4: Inclusives II: K^0, $K^{*\pm}$ and $K^{\pm}$

K^0 are easily found in complex hadronic events as they have a very clean signature.† Half of K^0 produced are K_S which have a proper decay length of 2.7 cm. Two thirds of these K_S decay into two charged π. Such K^0 decays can be identified by the two pion tracks which meet far from the main vertex of the event (Fig. 4.1). This procedure allows a very clean K_S signal to be found.

4.1 K^0 CUTS

None of the reconstruction cuts defined in the previous chapter are used. Candidate tracks are required to satisfy:

a) $|\cos\theta| \leq 0.8$ and

b) $r_{dca} \geq 1.0$mm – Almost all tracks from K_S decays which occur with the decay plane non-parallel to the z direction are expected to have impact parameters of order 1 cm.

Tracks passing the track cuts are then combined into charge zero pairs and the points at which the tracks intersect in the $x-y$ planes calculated. All of the calculations of track crossings and vertex constraints are done with a program package, VFINDP [18]. Of the two crossing points of the tracks in the $x-y$ plane, the one which implies a positive decay length and is nearest to the interaction point is chosen. The track momenta are corrected for energy loss in the material that the tracks traverse after the decay and combined to form the 4-vector of the

† Here K^0 means both K^0 and $\overline{K}^0$.

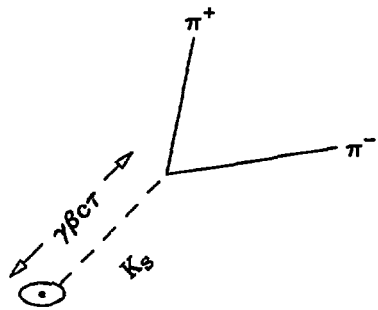

Figure 4.1: K_S decays to $\pi^+\pi^-$

'V'. Since in this analysis only K_S are of interest the two tracks are assumed to be pions. We require that:

a) the momentum vector of the 'V', extrapolated through the intersection of the 'V' tracks trace back to within 5 mm of the center of the beam spot.

b) the measured proper decay length $c\tau$ be greater than 5 mm. (In this calculation, the mass is that of the two pions and is not constrained to the K^0 mass.)

The tracks are then constrained to pass through a single point in space. As the z coordinates of tracks have large errors, this constraint changes the z and dip angles of the track but has little effect on the projection in the $x-y$ plane. The $\pi^+\pi^-$ pair mass is then calculated. Fig. 4.2 shows the distribution of masses.

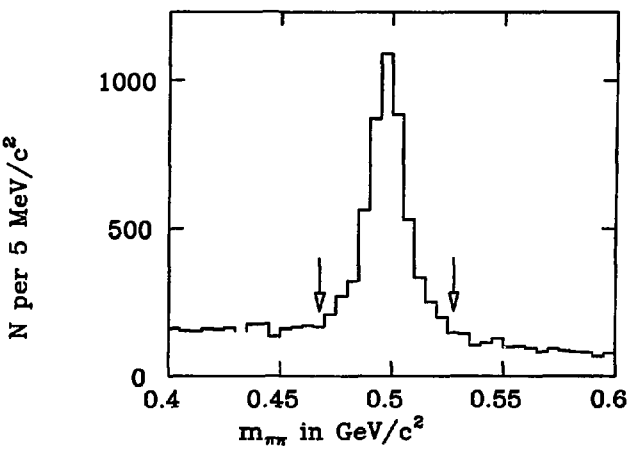

Figure 4.2: $m_{\pi\pi}$ after K_s selection cuts

The efficiency for finding K^0 in the 'BAD' and 'DC' data samples (described in Table 3.2) is substantially less than that for the better data samples. The RES sample also seems different from the VC and NEW data sets; the cross section is 2 sigma lower and the signal to noise is worse. To minimize unexplained

losses the K^0 rates are measured with only the VC and NEW data sets. These samples correspond to 105 pb^{-1}.

The number of K_S is estimated from a subtraction of the number of $\pi^+\pi^-$ pairs in the background regions $0.410 < m < 0.440$ GeV/c^2 and $0.560 < m < 0.590$ GeV/c^2 from that in the signal region $|m - m_{K^0}| < 0.030$ GeV/c^2. The number of $\pi^+\pi^-$ pairs in the signal region is 5683 and the number in the background regions is 1483. After background subtraction there are 4200 ± 85 K_S. This subtraction is done for several momentum bins to determine the differential cross section as a function of p, the K_S momentum.

Efficiency The efficiency for detecting the decay $K_S \to \pi^+\pi^-$ is estimated by application the same analysis procedure to simulated data produced by the Monte Carlo. 'V's are found with VFINDP and the background subtracted from the signal region. This gives $N(p)$ detected. The rest of the rate calculation is identical to the method used for the ρ^0 and K^{*0}. Radiative corrections are included.

Table 4.1a summarizes the number of K^0 per event as a function of p. Table 4.1b shows the invariant production rate as a function of $x \equiv E_K/E_{beam}$. The efficiency is very low for momenta less than 200 MeV/c or greater than 10 GeV/c and these regions are not included in the rate measurement. A correction for these missing regions is made with the Monte Carlo, which indicates that 1.6% of K^0 have momenta less than 200 MeV/c and 0.8% have momenta greater than 10 GeV/c. The fractional uncertainties in these corrections could be quite large but given the small sizes of the corrections the uncertainty introduced in the total rate is very small.

p in GeV/c	N	$\epsilon = \epsilon(K^0)/\epsilon$(hadron)	N per event in bin
0.20 – 0.30	38 ± 13	0.220	0.020 ± 0.007
0.30 – 0.40	86 ± 16	0.220	0.044 ± 0.008
0.40 – 0.50	103 ± 17	0.240	0.049 ± 0.008
0.50 – 0.60	117 ± 17	0.265	0.050 ± 0.007
0.60 – 0.70	143 ± 17	0.295	0.055 ± 0.007
0.70 – 0.80	102 ± 17	0.325	0.036 ± 0.006
0.80 – 0.90	129 ± 17	0.360	0.041 ± 0.005
0.90 – 1.00	153 ± 17	0.395	0.044 ± 0.005
1.00 – 1.25	412 ± 27	0.425	0.110 ± 0.007
1.25 – 1.50	416 ± 25	0.475	0.099 ± 0.006
1.50 – 1.75	352 ± 23	0.480	0.083 ± 0.006
1.75 – 2.00	292 ± 21	0.470	0.071 ± 0.005
2.00 – 2.50	495 ± 27	0.460	0.122 ± 0.007
2.50 – 3.00	408 ± 23	0.435	0.106 ± 0.006
3.00 – 3.50	244 ± 18	0.400	0.069 ± 0.005
3.50 – 4.25	288 ± 19	0.375	0.087 ± 0.006
4.25 – 5.00	176 ± 15	0.350	0.057 ± 0.005
5.00 – 6.00	124 ± 13	0.310	0.045 ± 0.005
6.00 – 7.00	66 ± 9	0.280	0.027 ± 0.004
7.00 – 8.50	36 ± 7	0.240	0.017 ± 0.003
8.50 – 10.00	23 ± 5	0.190	0.014 ± 0.003
0.20 – 10.00	4300 ± 85		1.242 ± 0.027
0.00 – 14.50			1.272 ± 0.028
2.00 – 14.50			0.555 ± 0.015

Table 4.1a: $K^0, \overline{K}^0$ per event as a function of p - Statistical errors only. The efficiency is that for finding a $K_S \rightarrow \pi^+\pi^-$ decay in a detected hadronic event.

x	$1/(\beta\sigma_H)d\sigma/dx$
0.038	14.18 ± 3.76
0.042	19.44 ± 3.51
0.046	15.73 ± 2.51
0.051	12.58 ± 1.91
0.056	11.33 ± 1.47
0.062	8.28 ± 1.42
0.068	8.84 ± 1.31
0.074	8.71 ± 1.11
0.085	7.52 ± 0.60
0.100	6.53 ± 0.51
0.117	5.07 ± 0.43
0.133	4.55 ± 0.43
0.159	3.73 ± 0.27
0.192	3.17 ± 0.25
0.226	2.23 ± 0.22
0.269	1.70 ± 0.16
0.320	1.10 ± 0.13
0.380	0.66 ± 0.09
0.449	0.39 ± 0.07
0.535	0.17 ± 0.04
0.638	0.13 ± 0.04

Table 4.1b: The invariant production rate $1/(\beta\sigma_H)\ d\sigma/dx$ for K^0 and $\overline{K}^0$.

Contamination The K^0 signal after background subtraction is not contaminated by Λ decays or γ conversions. Fig 4.3 shows the center of mass decay angle distribution for the K_S decay. The angle θ_{cm} is defined as the angle between the positive track in the K_S center of mass system and the K_S flight direction.

Λ decays and γ conversions would populate the regions near $\cos\theta_{cm} = \pm 1$. No significant contribution from other decays is evident.

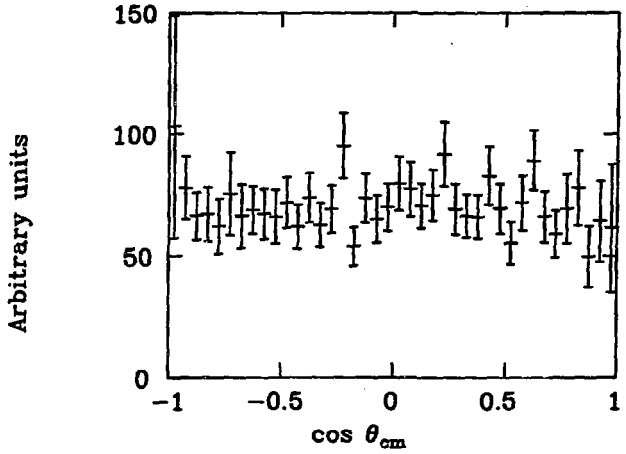

Figure 4.3: Back-ground subtracted distribution of K_S center of mass decay angles. The data have been corrected for the efficiency as a function of θ_{cm}.

4.2 SYSTEMATICS

There are several sources of systematic error in this measurement:

a) The Monte Carlo may not simulate the data perfectly; uncertainties in the reconstruction efficiency for individual tracks which come from

the beam interaction point are estimated to be around 3%. As the tracks which make up the K^0 do not come from the interaction point, the uncertainty per track for the K^0 may be higher. We estimate an error of 5% per track. As the K^0 requires 2 tracks, a conservative estimate of the uncertainty in the tracking efficiency is 10%.

b) The efficiency has a statistical error of order 3%.

c) The radiative correction, model dependence and hadron efficiency contribute an error of 5% as in the ρ^0 measurement.

The total systematic uncertainty in the production rate is thus estimated to be 12% and the number of $K^0, \bar{K}^0$ per event is $1.27 \pm .03 \pm .15$.

Several other experiments have published K^0 cross sections at center of mass energies near 29 GeV [19, 20, 21, 22]. Their results are summarized in Table 4.2

Experiment	reference	Date	Energy, GeV	K^0 per event
TASSO	[19]	1980	29.9-31.6	$1.4 \pm 0.3 \pm 0.14$
PLUTO	[20]	1981	30	1.40 ± 0.30
JADE	[21]	1983	30	$1.49 \pm 0.22 \pm 0.15$
JADE	"	1983	35	$1.45 \pm 0.08 \pm 0.15$
TPC	[22]	1984	29	$1.22 \pm 0.03 \pm 0.15$
Mark II	this dissertation	1984	29	$1.27 \pm 0.03 \pm 0.15$

Table 4.2: Comparison of K^0 cross section with other experiments

4.3 $K^{*\pm}$

We detect $K^{*\pm}$ by combining K_S from the full data sample with charged tracks and fitting the resulting $K_S\pi^\pm$ invariant mass distributions. The method used is very similar to the ρ^0/K^{*0} analysis but is somewhat simpler as there are no extraneous resonances to complicate the fit.

K_S candidates are selected by the cuts described in the previous sections. K_S candidates with masses less than 30 MeV/c^2 from the K^0 mass are constrained to that mass. All other 'K_S' are rejected as are mass constrained K_S with momenta less than 500 MeV/c. The $\pi^\pm$ are required to pass the same cuts as those used in the ρ^0 and K^{*0} analysis.

4.4 Fit Procedure

We obtain a smeared $K^{*\pm}$ resonance shape by generating $K^{*\pm}$ in the Monte Carlo and histogramming the detected masses in the same fashion as in the ρ^0 analysis. This shape reflects the detector resolution as well as the width of the resonance. The $K_S\pi^\pm$ mass distribution is then fit to this shape plus a quartic background function. $K_S\pi^\pm$ masses between 0.700 and 1.400 GeV/c^2 are included in the fit.

This fit is done for several momentum regions; the results are summarized in Table 4.3. Figure 4.4 shows the fit for all $p > 2$ GeV/c.

p, GeV/c	N_{K^*}	χ^2/dof
2.00-3.50	341± 93	40.3/30
3.50-5.00	213± 73	24.1/30
5.00-7.00	115± 45	22.9/30
7.00-10.0	30± 26	22.9/30
2.00-14.5	726±134	37.0/30

Table 4.3: Results of fits to the $K_S\pi$ mass spectrum. No corrections for K^* or K_S branching ratios is included.

4.5 CHECKS

Various checks of the fitting procedure have been performed:

Monte Carlo An identical analysis has been done for a Monte Carlo sample. There are 782 produced $K^{*\pm}$ which pass all of the cuts; the fit finds 833 $\pm$ 130 with a χ^2 of 20.3 for 30 degrees of freedom. This indicates a bias of $6 \pm 16\%$ due to the fitting procedure.

Null Signal The same analysis has been run on $K_S\pi^\pm$ pairs from the Monte Carlo which are known not to be from $K^{*\pm}$ decay. The fit finds -22 ± 116 $K^{*\pm}$ where none are expected.

Fit limits The lower limit on the $K\pi$ mass has been varied from 700 to 760 MeV/c^2; the number of $K^{*\pm}$ changes from 726±134 to 704±167. A change in the upper limit from 1400 to 1200 MeV/c^2 lowers the number of $K^{*\pm}$ found to 649±144.

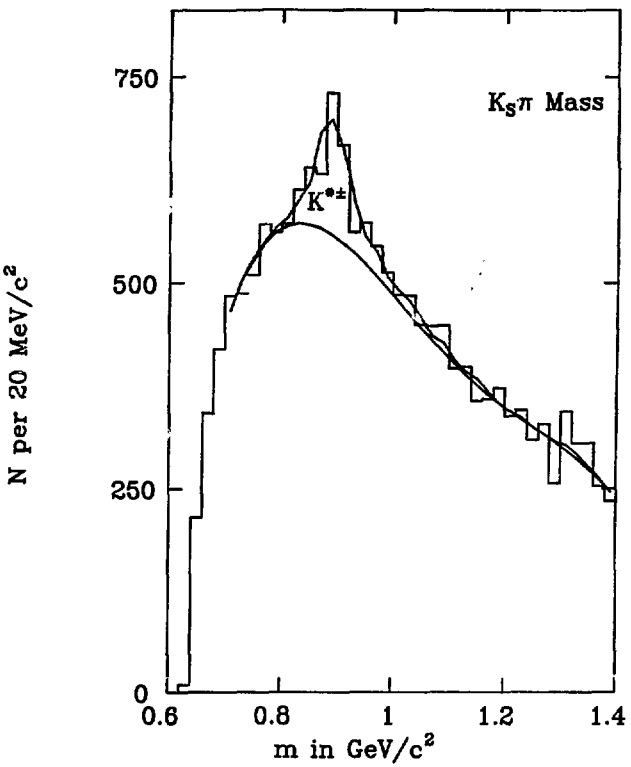

Figure 4.4: Fit to $K_S\pi$ mass spectrum for $p > 2$ GeV/c.

4.6 EFFICIENCY

The $K^{*\pm}$ reconstruction efficiency is estimated from the Monte Carlo. The 'fit' efficiency – obtained from a comparison of the results of a fit to the Monte Carlo sample with the produced number of $K^{*\pm}$ – is only 6% higher than the efficiency obtained from the simpler requirement that both the $\pi^{\pm}$ and the K_S be reconstructed. The 'fit' efficiency has a 16% statistical error due to the limited Monte Carlo statistics as noted above. In the analysis below the 'fit' efficiency is used and the 16% error in the efficiency is considered a systematic error.

As the full data sample is used in this analysis, the rates must be corrected for any inefficiency in this sample relative to the best sample. Correction factors are estimated from comparisons of the numbers of K^0 and $\pi^{\pm}$ detected per event in the NEW and VC samples with the numbers detected in the full sample. These correction factors are 89±2% for K^0 and 97±1% for $\pi^{\pm}$. The corrections show no momentum dependence. Table 4.4 summarizes the corrected rates per event and Figure 4.5a shows $1/(\beta\sigma_H)d\sigma/dx$ for K^0 and $K^{*\pm}$ from this experiment. Figure 4.5b compares the $K^{*\pm}$ rate with measurements by the JADE[17] and TPC[22] collaborations.

4.7 SYSTEMATICS

Contributions to the systematic errors on the K^* rate include the following:

- The efficiency has a statistical error of 16%.
- The error due to the event normalization and radiative corrections is estimated to be 5% as for the K^0.

p, GeV/c	N	$\epsilon(p)$	N per event nb	$1/(\beta\sigma_H)d\sigma/dx$
2.00-3.50	341± 93	0.088±0.014	0.122±0.033	1.31 ± 0.36
3.50-5.00	213± 73	0.094±0.015	0.072±0.025	0.73 ± 0.25
5.00-7.00	115± 45	0.085±0.013	0.043±0.017	0.32 ± 0.12
7.00-10.0	30± 26	0.085±0.013	0.011±0.010	0.054 ± 0.047
2.00-14.5	726±134	0.088±0.014	0.260±0.048	*

Table 4.4: $K^{*\pm}$ production rate as a function of p. The efficiencies include the K^* branching fraction but not the K^0 fractions.

- There is a 10% uncertainty in the K^0 tracking efficiency and an additional 3% for the pion. The total tracking efficiency error is thus 13%.

The estimated systematic error on the $K^{*\pm}$ rate found by adding these estimates in quadrature is 21%.

The total rate for $K^{*\pm}$ with $p_{K^*} \geq 2$ GeV is $0.260 \pm 0.047 \pm 0.055$ per event. This can be compared with the other results for $p \geq 2$ GeV/c summarized in Table 4.5. The $K^{*0} + \overline{K}^{*0}$ and the $K^{*\pm}$ rate are equal within errors.

	N per event
ρ^0	$0.254 \pm 0.030 \pm 0.050$
$K^{*0} + \overline{K}^{*0}$	$0.243 \pm 0.029 \pm 0.048$
$K^{*\pm}$	$0.260 \pm 0.047 \pm 0.055$
$K^0 + \overline{K}^0$	$0.555 \pm 0.015 \pm 0.066$

Table 4.5: Summary of production rates for $p \geq 2$ GeV/c.

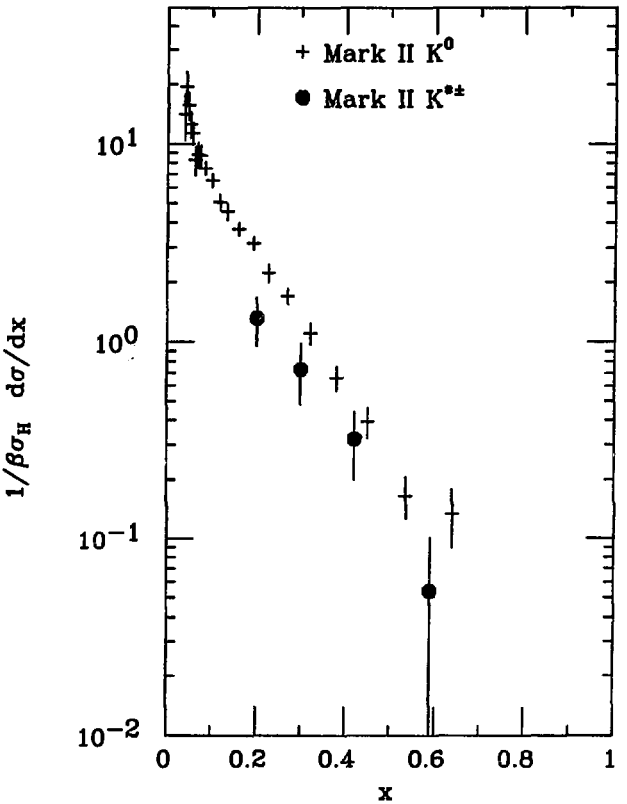

Figure 4.5a: $K^0 + \bar{K}^0$ and $K^{*\pm}$ production rates as a function of x. (Statistical errors only)

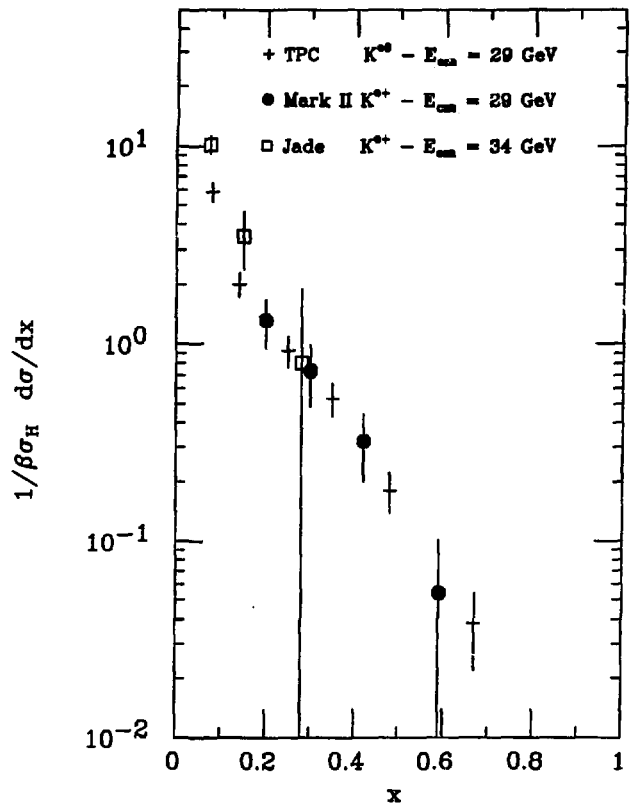

Figure 4.5b: $K^{*\pm}$ production rates as a function of x. (Statistical errors only)

4.8 $K^{\pm}$

The inclusive rate for $K^{\pm}$ production in e^+e^- annihilation at $\sqrt{s} \sim$ 30 GeV has been measured in several experiments. The TASSO collaboration has measured a total $K^{\pm}$ inclusive rate of 2.0 ± 0.2 $K^{\pm}$ per hadronic event at $\sqrt{s} = 34$ GeV using time of flight and Čerenkov particle identification [23]. The TPC collaboration has measured 1.35 ± 0.13 $K^{\pm}$ per event at $\sqrt{s} = 29$ GeV using dE/dx information [1].

Much of the disagreement between the two $K^{\pm}$ measurements arises in the low $x \equiv E_K/E_{beam}$ region where the Mark II time of flight system can identify $K^{\pm}$. We thus search for $K^{\pm}$ in the momentum range $0.3 < p < 0.9$ GeV/c.

The data samples used in this measurement are the VC, BAD and RES samples defined in Table 3.2 which correspond to a total integrated luminosity of 127 pb^{-1}. The NEW samples do not have good time of flight system calibration constants and are not used.

Hadronic events are selected in the usual manner. Tracks used in the kaon analysis are required to be well reconstructed as defined in Chapter 3 and in addition to have $|\cos\theta| < 0.5$. The track is required to hit a time of flight scintillator, produce a time measurement at both ends and be the only drift chamber track pointing at that scintillator. These cuts assure that the time of flight information is optimal; for such tracks the rms time resolution is 350psec and the z of the track determined by the time of flight system has an rms error of 8 cm.

Monte Carlo studies indicate that 25–50% of $K^{\pm}$ produced at momenta from 300–900 MeV/c decay before reaching the time of flight system. Kaons which decay usually cannot be properly fit with a single helical curve and are

probably not reconstructed at all or are reconstructed improperly. Poorly reconstructed tracks have bad r or z information and usually do not have hits beyond the decay point. The reconstruction cuts thus remove many decays in flight. In addition to the previous track cuts, at least one hit is required in the last 4 layers of the drift chamber and the z determined by the time of flight system is required to agree within 25 cm with that predicted by the drift chamber. These cuts lower the fraction of kaons accepted which decay in flight to 5–9% with most of the residual decays occurring within 50 cm of the scintillators where they have little effect on the measured velocity. Losses due to hadronic interactions in the material are less than 2%.

The number of kaons is extracted from the measured times of flight a fit of the distribution of the difference between the measured time, t_{meas}, and the expected time for a kaon, t^{K}_{exp}, in each of twelve 50 MeV/c momentum slices between 300 and 900 MeV/c. The expected time is given by:

$$t_{exp}(\ell, m, p) = \frac{\ell}{\beta c} = \frac{\ell}{c}\left(1 + \frac{m^2}{p^2}\right)^{\frac{1}{2}}$$

where ℓ is the path length, m is the mass and p is the momentum. Figure 4.6 shows the distribution of $t_{meas} - t^{K}_{exp}$ for all tracks in two typical momentum bins. The kaon contribution is centered around zero and reflects the resolution of the time of flight measurement, while contributions from $e^{\pm}$, $\pi^{\pm}$ and $p/\bar{p}$ are, in addition, widened by the spread in path lengths and momenta within each momentum bin. For example, a pion would have a measured time of

$$t_{meas} = \frac{\ell}{c}\left(1 + \frac{m_{\pi}^2}{p^2}\right)^{\frac{1}{2}} \pm \sigma_{TOF}$$

where σ_{TOF} is the spread due to the time of flight resolution. The difference between this t_{meas} and t^{K}_{exp} is a function of ℓ and p in addition to the TOF

resolution. The measured distribution of ℓ and p in the data are used to construct the distributions of $t_{exp} - t^{K}_{exp}$ for the mass hypotheses $e^{\pm}$, $\pi^{\pm}$ and $p/\bar{p}$. These distributions are then convoluted with a resolution function to produce fit functions which reproduce the expected contribution to $t_{meas} - t^{K}_{exp}$ of each mass hypothesis. The resolution function for the time of flight system is determined from tracks with $p > 3$ GeV/c and thus includes any non-gaussian tails. The relative normalizations of the fit functions are varied to fit the observed distribution of time of flight minus kaon time. Proton contributions are included only for $p > 700$ MeV/c.

Figure 4.6 shows such fits to two typical momentum slices. The same procedure has been performed on simulated data and reproduces the true number of $K^{\pm}$ to within 4%. As a check on the effects of any systematic momentum errors, the measured momenta for drift chamber tracks have been varied by 10 MeV/c, producing large changes in fit χ^2 but only 6% shifts in the measured numbers of kaons.

The momenta used to determine the slices are those measured at the drift chambers. The true momenta are somewhat higher due to energy loss in the material traversed by charged tracks. This correction ranges between 3 and 10 MeV/c and is included in the determination of x.

The numbers of $K^{\pm}$ found by this method are corrected for efficiency and initial state radiation to yield the numbers of $K^{\pm}$ per event. The efficiency for a kaon passing all of the cuts is determined from the Monte Carlo for each momentum slice. Studies of all charged tracks which yield good time of flight information – over 90% pions in this energy range – indicate that the requirement of a single hit in a counter and good z_{tof} information is only $86 \pm 2\%$ efficient for well-reconstructed tracks in the data as compared to the Monte Carlo. This factor

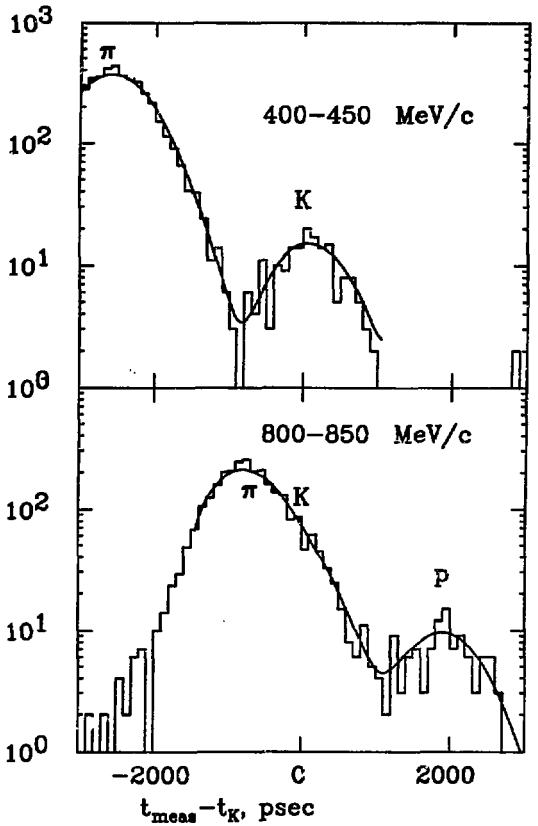

Figure 4.6: Distribution of measured times of flight for momentum slices $0.400 < p < 0.450$ GeV/c and $0.800 < p < 0.850$ GeV/c. The χ^2 for the fits are 40.1 for 43 degrees of freedom and 50.0 for 54 degrees of freedom respectively.

shows no variation with momentum. This is believed to be due to the absence of neutral particle interactions in the TOF system in the Monte Carlo which lowers the simulated occupancy of the counters. The efficiencies are corrected for this factor and for the measured losses in charged tracking efficiency in the BAD data samples. These efficiencies are then used to determine the numbers of kaons in the event sample. The normalization of the sample is done in the same fashion as for the other rate measurements.

As noted in Chapter 3 systematic errors due to uncertainties in the event efficiency and radiative corrections largely cancel in the ratio. The systematic error due to the efficiency calculation is thus dominated by the Monte Carlo simulation of individual track efficiencies and by the fit procedure. The drift chamber efficiency correction and model dependence yield an estimated systematic error of 6% for all charged tracks including variations in data sample quality. Kaons which do not decay in flight should behave like any other charged track. As decays in flight contribute 5–9% of the total detected kaons, even a 50% uncertainty in the efficiency for decaying tracks will only contribute 4% to the uncertainty in the total efficiency. The error due to the correction for differing time of flight efficiencies in the data and Monte Carlo is 2%. Combining the above estimates with the 4% uncertainty in to the fit procedure and the 6% uncertainty due to momentum measurement errors gives a systematic error of 12%.

Table 4.6 summarizes the results and Figure 4.7 compares them with the results from the TASSO [23] and TPC [1] collaborations. A measurement from TASSO at $\sqrt{s} = 22$ GeV is also shown. As both TASSO measurements are higher than the TPC and Mark II values the difference between the 29 and 34 GeV results cannot easily be interpreted as a beam energy dependent effect.

p, MeV/c	x	N per event	$\frac{1}{\beta\sigma_H}\frac{d\sigma}{dx}$
310-406	.0422	$0.0477 \pm 0.0029 \pm 0.0057$	$21.1 \pm 1.3 \pm 2.5$
406-504	.0464	$0.0555 \pm 0.0040 \pm 0.0067$	$18.0 \pm 1.3 \pm 2.2$
504-604	.0513	$0.0623 \pm 0.0045 \pm 0.0075$	$16.5 \pm 1.2 \pm 2.0$
604-703	.0565	$0.0693 \pm 0.0053 \pm 0.0083$	$15.8 \pm 1.2 \pm 1.9$
703-803	.0621	$0.0674 \pm 0.0072 \pm 0.0081$	$14.0 \pm 1.5 \pm 1.7$
803-902	.0680	$0.0585 \pm 0.0076 \pm 0.0070$	$11.5 \pm 1.5 \pm 1.4$

Table 4.6: Summary of $K^{\pm}$ cross section. The momentum bins reflect energy loss corrections appropriate to kaons

Fig 4.8 shows a comparison of $K^{\pm}$ and $K^0 + \overline{K}^0$ rates for $x < 0.1$. Over the range $0.04 < x < 0.07$ where both rates are measured the $K^0 + \overline{K}^0$ rate is $0.76 \pm 0.06 \pm 0.13$ of the $K^{\pm}$ rate.

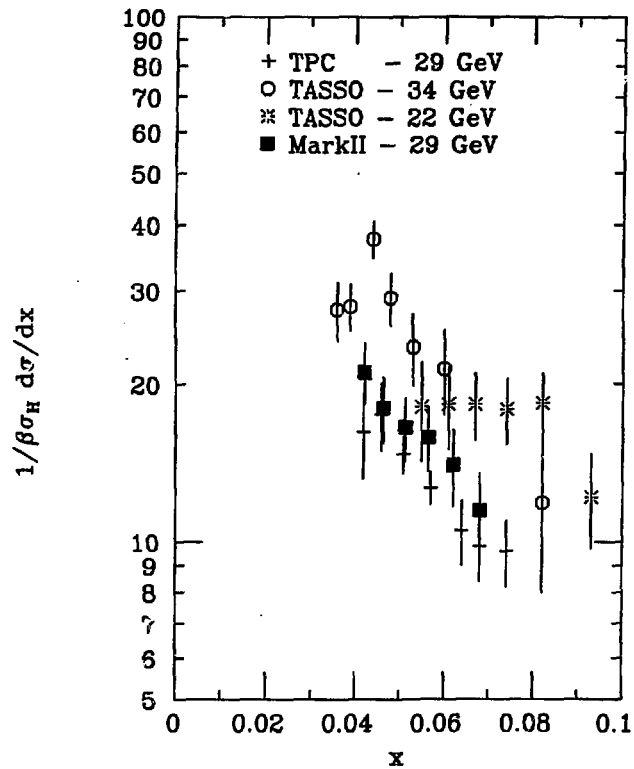

Figure 4.7: The $K^{\pm}$ differential rate from the present experiment compared with the TASSO and TPC results. Systematic errors are included in the error bars.

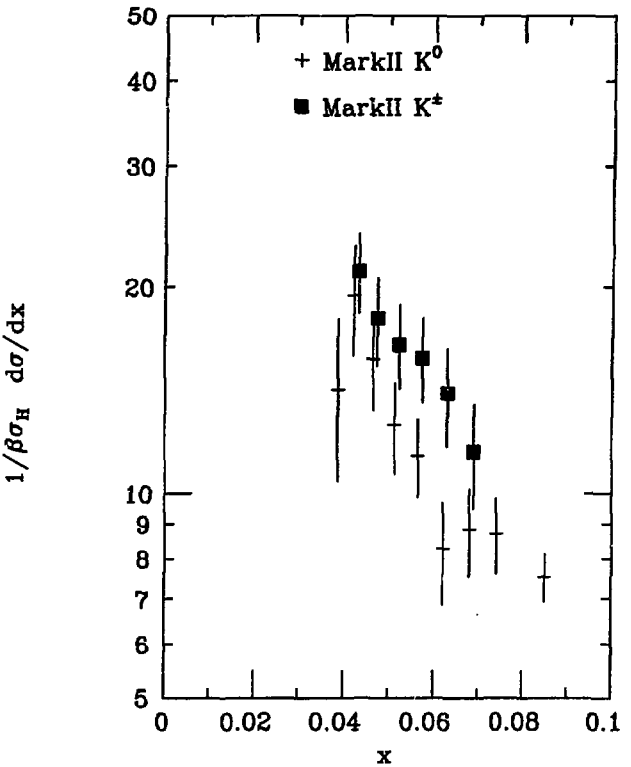

Figure 4.8: $K^{\pm}$ and $K^0 + \bar{K}^0$ differential rates for $x < 0.1$.

Chapter 5: Suppression of Strange and Vector Mesons

In e^+e^- annihilation, mesons are produced from the hadronization (or 'fragmentation') of the initial $q\bar{q}$ pair. In most models of fragmentation, additional $q\bar{q}$ pairs are pulled from the vacuum and combine with the initial $q\bar{q}$ pair – and each other – to form mesons and baryons. Figure 5.1 illustrates such a process. These 'primary' mesons, or their decay products, make up the observed meson samples. Hadronization models differ widely in the dynamics invoked to produce the $q\bar{q}$ pairs from the vacuum; in this Chapter I attempt to extract information about hadronization from the measured meson rates without relying on a particular model.

5.1 Suppression of Strange Vector Mesons

K^{*0} and ρ^0 differ only in the substitution of an s (strange) quark for a d (down) quark. The ratio of K^{*0} to ρ^0 production should thus be a sensitive probe of the differences between s and d quarks in fragmentation.† As the ρ and K^* masses are similar, the comparison can be done for the momentum range $p > 1$ GeV without extrapolation to zero momentum. (Such an extrapolation is needed for mesons with differing masses as it is not known whether rates should be compared as a function of energy, momentum or some other variable.) In

† ρ^0 are believed to have quark content $\frac{1}{\sqrt{2}}(|u\bar{u}\rangle - |d\bar{d}\rangle)$ while K^{*0} are $|d\bar{s}\rangle$. The u and d quarks have nearly equal small masses and the s quark is somewhat heavier. This mass difference breaks SU(3) flavor symmetry.

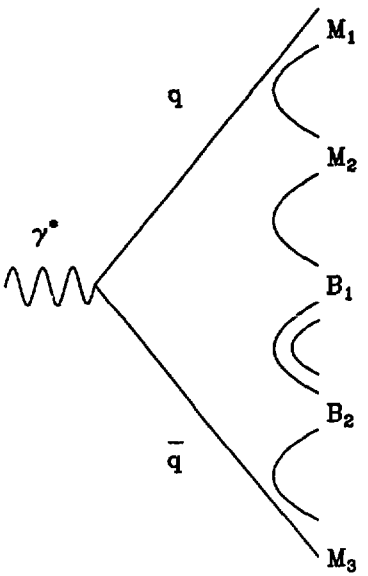

Figure 5.1: Hadronization of a $q\bar{q}$ pair from e^+e^- annihilation. Additional quark pairs come from the vacuum to form mesons (M) and baryons (B).

addition, it is believed that most mesons produced in fragmentation are pseudoscalar or vector particles as only these states can be produced in an s-wave by spin $\frac{1}{2}$ quarks. This implies that almost all vector particles seen in e^+e^- annihilation are 'primary' rather than decay products of some heavier mesons.

If most vector particles are primary, the corrections for decays are small and do not require a complicated Monte Carlo simulation. In the following sections I describe a simple model used to calculate the small corrections needed to extract from the measured rates the ratio of K^{*0} to ρ^0 resulting from pure fragmentation.

5.2 CORRECTIONS

To isolate the fragmentation effects the measured rates must be corrected for decays and leading quark effects which also contribute to the production rates. These effects are:

i. The dominance of leading u and c quarks from the initial $e^+e^- \rightarrow q\bar{q}$ vertex. This raises the ρ^0 rate relative to K^{*0} rate.

ii. Weak decays of D, F and B mesons.

Corrections for these effects will be treated separately below.

Leading quark contribution Due to the $e^+e^- \rightarrow \gamma^* \rightarrow q\bar{q}$ vertex, events occur with probability 4/11 for $u\bar{u}$ and $c\bar{c}$ and 1/11 for $d\bar{d}$, $s\bar{s}$ and $b\bar{b}$. This creates differences in the number of ρ^0, K^{*0} and $K^{*\pm}$ which are not due to fragmentation effects. A simple model can be used to estimate the numbers of vector mesons expected from each flavor of leading quark.

The production of mesons in fragmentation has generally been described by two parameters f_v, the fraction of vector particles produced, γ_s, the suppression of mesons containing strange quarks relative to those containing only up and down quarks and a function $f(z)$ which determines the distribution of the initial quark's energy among the primary mesons. The precise definitions of f_v and γ_s are

$$f_v = \frac{N_{\text{vector}}}{N_{\text{vector}} + N_{\text{pseudo-scalar}}}$$

and

$$\gamma_s = \frac{N_{s-\text{quarks}}}{N_{u-\text{quarks}}} = \frac{N_{s-\text{quarks}}}{N_{d-\text{quarks}}}$$

where N represents the number of primary mesons of a given type. These parameters are discussed further in sections 3.5 and 6.1. In the limit that there are no mass differences between mesons and SU(3) flavor symmetry holds, f_v would be $\frac{3}{4}$ as vector particles have 3 spin states and γ_s would be 1.

These parameters have been determined in the past by comparison of production rates for vector and strange mesons with the rates predicted by a Monte Carlo model for various values of the relevant parameter. The resulting parameter values are dependent on the model used. Typical values for these parameters are $f_v = 0.50$, $\gamma_s = 0.30$ and $f(z) = (1-z)^{0.7}$. Although these values are model dependent they should suffice for an estimate of leading quark effects.

Let p_s be the probability of producing an $s\bar{s}$ instead of a $u\bar{u}$ or $d\bar{d}$ in fragmentation ($\gamma_s = p_s/p_u$). As an example I will work out the probability per event for a $d\bar{d}$ to produce a leading K^{*0}: 1/11 for the $d\bar{d}$ vertex, 2 for the two leading quarks, f_v for producing a vector particle, and p_s for getting the $\bar{s}$ quark needed to make a $d\bar{s}$ pair. The probability for $d\bar{d} \rightarrow$ leading $K^{*0}, \bar{K}^{*0}$ is thus $\frac{1}{11} f_v 2 p_s$.

Charm The situation for charm and bottom is somewhat trickier as there is a weak decay involved. Although the inclusive branching fractions for charm decays into vector mesons have not been measured explicitly it is possible to set limits from the known exclusive channels. I assume that the branching ratios determined from D decays reflect the total charm branching ratios as there is no information for F decays.

Due to constraints from energy and charge conservation there are few plausible decay modes for D mesons into vector mesons. Many of these modes have been measured explicitly. Tables 5.1a and 5.1b summarize the limits. Particle Data Group values [24] and new numbers presented by the Mark III collaboration at the SLAC Summer Institute [25] are used in the calculations. The measured errors have been added in quadrature to produce plausible ranges for the branching fractions. All upper limits from the Particle Data group compilation are 90% confidence limits but have been treated as if they were 1 sigma errors for simplicity.

A measurement by the HRS collaboration [26] indicates that the ratio of D^0 to D^+ production at $\sqrt{s} = 29$ GeV is 2.3 ± 1.2. The branching ratio for $D \rightarrow \overline{K}^{*0} + X$ is thus between 3 and 14% and $B(D \rightarrow \rho^0 + X)$ is between 3 and 10%. (These are approximate 1 sigma limits.)

Bottom decays $b \rightarrow c d \bar{u}$, I assume that the c quark decays in the normal fashion and treat the d and $\bar{u}$ as leading quarks. As there are few $b\bar{b}$ events these assumptions do not have much effect on the result.

mode	limit	source
$D^0 \to \bar{K}^{*0}\pi^0$	$1.4^{+2.3}_{-1.4}\%$	PDG
$D^0 \to \bar{K}^{*0}\pi^+\pi^-$	$< 2.3\%$	PDG
$D^0 \to \bar{K}^{*0}\pi^0\pi^0$	unknown	
If $\bar{K}^{*0}\pi^0\pi^0 \sim \bar{K}^{*0}\pi^-\pi^+$ then $D^0 \to \bar{K}^{*0} + X$ is $0-7\%$.		
$D^+ \to \bar{K}^{*0}\pi^+$	$< 3.7\%$	PDG
$D^+ \to \bar{K}^{*0}\pi^+\pi^0$	$< \frac{3}{2}B(D^+ \to K^-\pi^+\pi^+\pi^0)$	
	$= \frac{3}{2}(4.3 \pm 1.9\%)$	Mark III
$D^+ \to \bar{K}^{*0}\ell\nu$	$17 \pm 7\%$	Mark III
	(semi-leptonic is $50 \pm 20\%$ K^*)	
$D^+ \to \bar{K}^{*0} + X$ is $10-30\%$		

Table 5.1a: Limits on $D \to \bar{K}^{*0} + X$. Contributions from modes with more than two pions are expected to be small due to phase space.

5.3 VECTOR MESONS FROM FRAGMENTATION

Table 5.2 summarizes the contributions of leading quarks to the measured rates per event.

These are the total contributions from leading quarks; a simple minded integration of the preferred fragmentation function $f(z) = (1-z)^{\cdot 7}$ indicates that 85 ± 10 % of leading K^* or ρ have $p \geq 1$ GeV/c. Monte Carlo calculations indicate that 80% of vector mesons from charm decays have $p > 1$ GeV/c.

For reasonable parameter values of $f_v = 0.5$ and $p_s = 0.15$ leading u, d and s quarks contribute 0.12 ρ^0 and 0.05 K^{*0} and $\bar{K}^{*0}$ per event with $p > 1$ GeV/c. Charm decays contribute an additional 0.03-0.07 ρ^0 and 0.03-0.10 K^{*0} and $\bar{K}^{*0}$

mode	limit	source
$D^0 \to \bar{K}^0 \rho^0$	$0.9 \pm 0.4\%$	Mark III
$D^0 \to K^- \pi^+ \rho^0$	$3.9^{+1.3}_{-1.6}\%$	PDG
$D^0 \to \bar{K}^0 \pi^0 \rho^0$	unknown	
If $\bar{K}^0 \pi^0 \rho^0 \sim K^- \pi^+ \rho^0$ then $D^0 \to \rho^0 + X$ is $5 - 11\%$.		
$D^+ \to \bar{K}^0 \pi^+ \rho^0$	$< B(D^+ \to \bar{K}^0 \pi^+ \pi^- \pi^+)$ $= 6.3 \pm 1.8\%$	Mark III
$D^+ \to \rho^0 + X$ is $0 - 8\%$.		

Table 5.1b: Limits on $D \to \rho^0 + X$. Modes with more than two pions are expected to be small due to phase space.

per event with momenta greater than 1 GeV/c. These estimates can be used to find the number of vector particles from fragmentation alone.

After subtraction of the contributions from leading quarks and charm decays, there are $0.27 \pm 0.04 \pm 0.08$ ρ^0 and $0.30 \pm 0.05 \pm 0.09$ $K^{*0} + \bar{K}^{*0}$ from fragmentation per event with $p > 1$ GeV/c. The ratio of $K^{*0} + \bar{K}^{*0}$ to ρ^0 is 1.12 where flavor symmetry would predict 2. This indicates a relative suppression for strange vector mesons of 0.56 and corresponds to a p_s for vector particles of 0.22.

A value for p_s of 0.15 was used in the calculation of the leading quark contributions. With the improved value of 0.22, the number of ρ^0 changes to $0.28 \pm 0.04 \pm 0.08$ and the number of $K^{*0} + \bar{K}^{*0}$ changes to $0.29 \pm 0.05 \pm 0.09$ per event with $p > 1$ GeV/c. The ratio of $K^{*0} + \bar{K}^{*0}$ to ρ^0 becomes $1.04 \pm 0.24 \pm 0.25 \pm 0.20$ where the first error is statistical, the second reflects the systematic error from the measurement and the third reflects the error in the leading quark and charm

Leading flavor	Number of ρ^0	Number of $K^{*0} + \overline{K}^{*0}$	Number of $K^{*\pm}$
u	$2\frac{4}{11} f_v \frac{p_u}{2}$	none	$\frac{4}{11} f_v 2p_s$
d	$2\frac{1}{11} f_v \frac{p_d}{2}$	$\frac{1}{11} f_v 2p_s$	none
s	none	$\frac{1}{11} f_v 2p_d$	$\frac{1}{11} f_v 2p_u$
c	$\frac{4}{11} 2B(c \to \rho^0 + X)$	$\frac{4}{11} 2B(c \to K^{*0} + X)$	$\frac{4}{11} 2B(c \to K^{*-} + X)$
$b \to c\bar{d}\bar{u}$			
c produces	$\frac{1}{11} 2B(c \to \rho^0 + X)$	$\frac{1}{11} 2B(c \to \overline{K}^{*0} + X)$	$\frac{1}{11} 2B(c \to K^{*-} + X)$
d produces	$2\frac{1}{11} f_v \frac{p_d}{2}$	$\frac{1}{11} f_v 2p_s$	none
$\bar{u}$ produces	$2\frac{1}{11} f_v \frac{p_u}{2}$	none	$\frac{1}{11} f_v 2p_s$
Total	$\frac{1}{11} f_v(4p_u + 1p_d) +$ $\frac{10}{11} B(c \to \rho^0 + X) +$ $\frac{1}{11} f_v(p_u + p_d)$	$\frac{2}{11} f_v(p_d + p_s) +$ $\frac{10}{11} B(c \to \overline{K}^{*0} + X) +$ $\frac{2}{11} f_v(p_s)$	$\frac{2}{11} f_v(4p_s + p_u) +$ $\frac{10}{11} B(c \to K^{*-} + X) +$ $\frac{2}{11} f_v(p_s)$

Table 5.2: Leading quark contributions.

subtractions. Most of the third error comes from the charm subtractions. The relative suppression of strange vector mesons is thus $0.52 \pm 0.12 \pm 0.16$.

In this analysis I have assumed that there are no non-charm decay contributions to the ρ^0 and K^{*0} rates. For the K^{*0} this is a good assumption as there are no light pseudo-scalar or vector mesons which decay to K^*. The η', however, decays to $\rho^0\gamma$ with a branching fraction of 30%. As no measurement of the η' production rate in e^+e^- annihilation near $\sqrt{s} = 30$ GeV has been reported the contribution must be estimated theoretically. As the η' mass is close to that of the ρ^0 and K^{*0}, one would naively expect the production rate to be around 1/3 of the ρ^0 rate due to spin factors.

The η' is a mixture of flavor singlet and octet states. From the mixing angle of -10° derived from the Gell-Mann-Okubo mass formula, the quark content of the η' is:

$$|\eta'\rangle = \frac{1}{\sqrt{6}}(1.22|u\bar{u}\rangle + 1.22|d\bar{d}\rangle + 1.74|s\bar{s}\rangle),$$

while the quark content of the ρ^0 is:

$$|\rho^0\rangle = \frac{1}{\sqrt{2}}(|u\bar{u}\rangle - |d\bar{d}\rangle).$$

If we assume that flavor singlet mesons are not suppressed relative to octet mesons except by the strangeness suppression and that p_s is 0.22 and the spin factor is 3, the ratio of primary η' to ρ^0 should be 0.21. This implies that 7% of the ρ^0 from hadronization come from η' decay. If this additional contribution is subtracted from the measured ρ^0 rate the strange vector meson suppression becomes $0.57 \pm 0.12 \pm 0.17$.

This suppression is less pronounced than the strangeness suppressions of order 0.3 estimated by this and other experiments [21] from a comparison of the K^0 rate with Monte Carlo models. This measurement of the strangeness suppression is described in the next chapter.

5.4 VECTOR FRACTION FOR STRANGE MESONS

The vector fraction for strange mesons can also be estimated by a method similar to that used for the K^{*0} to ρ^0 ratio. This estimate is model dependent as the K^{*0} rate must be extrapolated to zero momentum for comparison with the K^0 rate.

There are 3 contributions to the ratio which must be taken into account:

- Extrapolation of the K^{*0} rate to zero momentum. The Field-Feynman Monte Carlo indicates that 67% of all K^{*0} have momenta greater than

1 GeV/c. This implies a total K^{*0} rate of $0.62 \pm 0.07 \pm 0.15$ per event; The systematic error includes an extrapolation uncertainty of 0.10.

- Charm decays contribute 0.08 ± 0.05 K^{*0} per event. If the Particle Data group [24] values for D branching ratios are combined with the HRS [26] estimate of the D^0 to D^+ ratio at 29 GeV, the charm branching ratio into K^0 is $37 \pm 9\%$. The contribution of charm to the K^0 rate is thus 0.33 ± 0.08 K^0 per event.
- K^* decays. The contribution to the K^0 rate from K^* decays is equal to the total K^{*0} rate if the $K^{*\pm}$ and K^{*0} production rates are assumed to be equal.

As K^{*0} and K^0 have the same quark content, no leading quark corrections are needed. The charm-subtracted K^{*0} rate is thus $0.54 \pm 0.07 \pm 0.16$ per event and the charm-subtracted K^0 rate is $0.94 \pm 0.03 \pm 0.18$. The number of primary K^0 after correction for K^{*0} decay is $0.40 \pm 0.08 \pm 0.24$ per event. The ratio of K^{*0} to $K^{*0} + K^0$ is thus $0.57 \pm 0.08 \pm 0.20$. This implies that $\sim 60\%$ of strange mesons are vectors.

5.5 PRIMARY PION RATE

The numbers of primary ρ^0, K^{*0} and K^0 have been estimated in the preceding sections. These estimates are reasonably model independent, except for the assumption that mesons can only be pseudo-scalars or vectors. With this assumption, and the assumption that states of similar mass and quantum numbers such as ρ^0 and ω are produced in equal numbers in hadronization, the primary pion rate can be estimated. This estimate involves many corrections which will each be treated individually below and then summarized in Table 5.3.

Branching fractions are taken from the Particle Data Group compilation [24] except where otherwise noted.

The total $\pi^{\pm}$ rate has been measured to be 10.7 ± 0.6 by the TPC collaboration [1]. The chief contributions to the $\pi^{\pm}$ rate are:

i. Charm decay: The mean charged multiplicity for charm decay was measured by the Mark II collaboration at SPEAR [6]. The charged multiplicity for D^0 decay was found to be 2.46 ± 0.15 and for D^+ decay, 2.16 ± 0.15. As D^0 are more common than D^+ at PEP, the mean charge multiplicity for charm decays at PEP is estimated to be 2.36 ± 0.15. Charged kaons should contribute 0.31 ± 0.10 and leptons, 0.13 ± 0.06. The number of $\pi^{\pm}$ for each charm decay is thus 1.92 ± 0.19. This number includes $\pi^{\pm}$ from K^0 decay. There are 10/11 charmed particles per event including the charm from B meson decays. The number of $\pi^{\pm}$ per event resulting from charm decay is thus 1.75 ± 0.17.

   D^{*+} decays to $D^0\pi^+ \sim 50\%$ of the time. This contributes another 0.18 ± 0.04 $\pi^{\pm}$ per event from charmed mesons.

ii. B meson decay: The mean charge multiplicity for B decay is 5.4 ± 0.4. Almost half of this is from the charm decays which have already been counted. The remaining mesons are mainly $\pi^{\pm}$ with the exception of 0.26 ± 0.03 leptons and an unknown small number of $K^{\pm}$ and protons. Each B meson thus produces 2.78 ± 0.43 charged pions in addition to the products of charm decay. There are 2/11 B mesons per event, yielding 0.51 ± 0.08 $\pi^{\pm}$ per event.

iii. η decay: The JADE collaboration [27] has measured an η production rate of $0.72 \pm 0.10 \pm 0.18$ per event at 34 GeV. Around 30% of η decays

yield charged π pairs, resulting in a contribution to the measured $\pi^{\pm}$ rate of 0.43 ± 0.12 per event.

iv. η' decays: The η' rate was estimated above to be 1/5 of the ρ^0 rate. For the extrapolated ρ^0 rate of $0.67 \pm 0.07 \pm 0.09$ derived in Chapter 3, this implies an η' rate of 0.13 ± 0.02 per event. The decay of η' yields around 1 $\pi^{\pm}$ and 0.3 ρ^0 or a total of 0.21 ± 0.03 $\pi^{\pm}$ per event including the products of the ρ^0 decay.

v. Vector meson decays: The extrapolated ρ^0 rate is 0.67 ± 0.15, including an extrapolation error of 0.10. This includes D and η' decay products which have already been accounted for. As noted above, the branching fraction for charm into ρ^0 is $3 - 10\%$. If this contribution and the η' contribution are subtracted out, the corrected number of ρ^0 per event is 0.56 ± 0.16 per event. This should be the 'primary' rate from pure hadronization. If equal production of $\rho^{\pm}$, ρ^0 and ω is assumed, the resulting number of $\pi^{\pm}$ is 3.36 ± 0.96.

K* decays also contribute an average of $2/3$ $\pi^{\pm}$ per decay. The number of K^{*0} per event from hadronization was estimated above to be 0.54 ± 0.16 after charm subtraction. If an equal number of $K^{*\pm}$ are assumed, K* decays contribute 0.72 ± 0.21 $\pi^{\pm}$ per event. The $\pi^{\pm}$ from K^0 decay will be accounted for in the K^0 contribution.

vi. K^0 decays: There are 0.94 ± 0.18 K^0 per event exclusive of those already accounted for in charm decays. Each K^0 decay will contribute $2/3$ $\pi^{\pm}$ for a total contribution of 0.63 ± 0.12 per event.

vii. Baryon decays: The strange baryons Λ, Σ and Ξ can contribute $\pi^{\pm}$. If the *primary* Σ rates are assumed to be equal to the primary Λ rate and the unpublished total Λ rate of 0.22 ± 0.03 from this experiment is used,

there are 0.08 ± 0.02 each of primary Λ, Σ^0 and $\Sigma^\pm$ per event. The number of doubly strange baryons Ξ has been measured by the TASSO collaboration [29] as 0.03 ± 0.01 $\Xi^\pm$ per event. If non-octet baryons are ignored, the contribution of baryon decays to the $\pi^\pm$ rate is 0.26 ± 0.04 per event.

Table 5.3 summarizes these contributions.

process		number of $\pi^\pm$ per event
measured number		10.7 ± 0.6
Charm decay		1.93 ± 0.18
Bottom decay		0.51 ± 0.08
η decay		0.43 ± 0.12
η' decay		0.21 ± 0.03
Vector meson decays:	ρ^0, $\rho^\pm$, ω	3.36 ± 0.96
	K^*	0.72 ± 0.21
K^0 decay		0.63 ± 0.12
Baryon decay	Λ, $\Sigma^\pm$	0.26 ± 0.04
Total decay		8.05 ± 1.02
Primary $\pi^\pm$	= measured − decay	2.65 ± 1.18

Table 5.3: Contributions to the measured $\pi^\pm$ rate. The total rate was measured by the TPC collaboration [1].

The assumptions used above were that the primary mesons rates are isospin symmetric and that events are made up of pseudo-scalar and vector mesons and of spin-$\frac{1}{2}$ baryons only. With these assumptions, the composition of the average hadronic event can be estimated. (See Table 5.4.)

Particle	number per event	source of estimate
Light pseudo-scalar		
$\pi^{\pm}$	2.65 ± 1.18	this chapter
π^0	1.32 ± 0.59	$= \frac{1}{2}\pi^{\pm}$
η	0.64 ± 0.21	JADE minus η' decay
$K^0 + \overline{K}^0$	0.40 ± 0.25	this chapter
$K^{\pm}$	0.40 ± 0.25	$= K^0$
η'	0.13 ± 0.03	$= \frac{1}{5}\rho^0$
sub-total	5.54 ± 1.85	
Light vectors		
ρ^0	0.56 ± 0.16	this chapter
ω	0.56 ± 0.16	$= \rho^0$
$\rho^{\pm}$	1.12 ± 0.32	$= 2\rho^0$
$K^{*0} + \overline{K}^{*0}$	0.54 ± 0.16	this chapter
$K^{*\pm}$	0.54 ± 0.16	$= K^{*0}$
ϕ	0.08 ± 0.02	TPC [28]
sub-total	3.40 ± 0.72	
total light mesons	8.94 ± 1.37	

Table 5.4: Contents of a hadronic event

Particle	number per event	source of estimate
Charm and Bottom		
Charm mesons and baryons	$\frac{8}{11}$	leading c quarks
B mesons and baryons	$\frac{2}{11}$	leading b quarks
sub-total	0.91	
Baryons		
Λ	0.08 ± 0.02	measured rate - decays
Σ^0	0.08 ± 0.02	$= \Lambda$
$\Sigma^{\pm}$	0.16 ± 0.02	$= \Lambda + \Sigma^0$
p+$\bar{\text{p}}$	0.38 ± 0.10	0.60 ± 0.08 from TPC[1]
		$-$ decays
n+$\bar{\text{n}}$	0.38 ± 0.10	same as proton
$\Xi^{\pm}$	0.03 ± 0.01	TASSO [29]
$\Xi^0 + \bar{\Xi}^0$	0.03 ± 0.01	$= \Xi^{\pm}$
sub-total	1.08 ± 0.20	
total particles	10.9 ± 1.4	

Table 5.4: (continued)Contents of a hadronic event

The numbers for $\pi^{\pm}$, K^0, ρ^0 and K^{*0} determined in this chapter can be used to define ratios (of which 3 are independent.) Where the statistical errors are much smaller than the systematic errors, only the combined error is quoted. These ratios are:

F_v^{ns}, the ratio of non-strange vector mesons to all non-strange mesons. This ratio can be approximated by,

$$F_v^{ns} = \frac{\rho^0}{\rho^0 + \frac{1}{2}\pi^{\pm}} = 0.30^{+0.17}_{-0.12}$$

F_v^s, the ratio of strange vector mesons to all strange mesons. This was evaluated in the previous section from K^0 and K^{*0} rates as $F_v^s = 0.57 \pm 0.08 \pm 0.20$

F_v, the ratio of all vector mesons to all mesons. This ratio can be approximated by,

$$F_v = \frac{\omega^0 + K^{*0} + \overline{K}^{*0}}{2\rho^0 + \pi^\pm + K^0 + \overline{K}^0 + K^{*0} + \overline{K}^{*0}}$$
$$= 0.35 \pm 0.13$$

R_s^v, the ratio of strange vector mesons to non-strange vector mesons. This was evaluated in section 5.3 of this chapter as $R_s^v = 0.57 \pm 0.12 \pm 0.17$.

R_s^{ps}, the ratio of strange pseudo-scalars to non-strange pseudo-scalars. This is,

$$R_s^{ps} = \frac{K^0 + \overline{K}^0}{\pi^\pm}$$
$$= 0.15^{+0.13}_{-0.10}$$

R_s, the ratio of all strange to all non-strange mesons. This is,

$$R_s = \frac{K^0 + \overline{K}^0 + K^{*0} + \overline{K}^{*0}}{2\rho^0 + \pi^\pm}$$
$$= 0.25 \pm 0.10$$

This notation for the ratios is designed to prevent confusion with the Monte Carlo parameters, f_v and γ_s which correspond to F_v and R_s. The Monte Carlo parameters are defined only within the context of an individual model and caution should be used in comparing them with numbers measured by other methods. In the next chapter the Field-Feynman model is used to evaluate these parameters.

The rates for the primary production of mesons derived in this Chapter are sensitive to the assumptions used in the subtraction of decays. The presence of tensor or scalar mesons in significant numbers cannot be ruled out with existing information and would have large effects on the primary meson counts.

Chapter 6: Comparisons with Specific Models.

Monte Carlo models of hadronization, such as the Field-Feynman [12] and LUND [30] models include parameters analogous to the F_v and R_s measured in the last chapter. In this chapter I use the measured rates for ρ^0, K^0 and K^* production to obtain values for the parameters used in the Field-Feynman model described in Chapter 3. This model is not intended to describe the physics of fragmentation at a fundamental level but does provide a useful parametrization of the data.

6.1 FIELD-FEYNMAN PARAMETERS

The quantities relevant to meson production rates are the number, M, of primary particles produced in fragmentation, the fraction, f_v, of these particles which are vector mesons (if they have enough energy), and the fraction, p_s which are strange. The model allows a calculation of the average numbers of mesons per event as a function of these parameters.

The number of primary particles is not an explicit parameter of the model; the model uses the fragmentation function $f(z)$ instead. This function determines the share of energy that each meson acquires from its parent quark and, indirectly, the total number of primary particles produced. For example, if $f(z)$ causes each meson to receive a large fraction of the available quark energy, the number of mesons produced for a fixed event energy will be small. M and $f(z)$ are thus strongly correlated. The fraction of vector particles can also have

a small effect on M as vector mesons require more energy than pseudo-scalars due to their higher masses. Figure 6.1 illustrates the dependence of M on the fragmentation function $f(z) = (1-z)^r$. The parameter r will be used instead of M for the rest of this analysis.

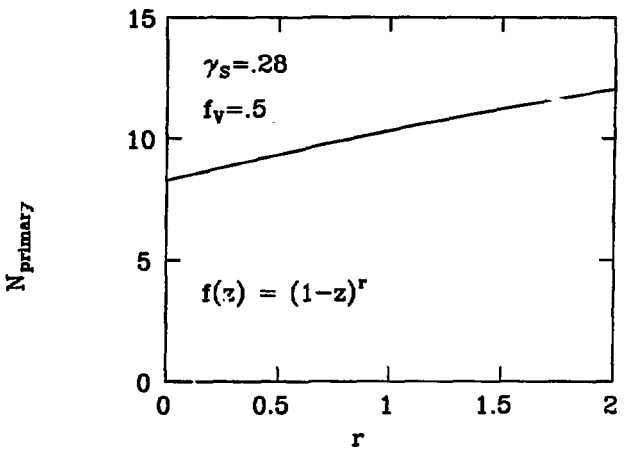

Figure 6.1: Dependence of the number of primary particles per event on the fragmentation function $f(z) = (1-z)^r$.

The parameters f_v and γ_s are not the same as F_v and R_s because of the nature of the hadronization algorithm. The parameters are used to choose between meson types only if the meson energy is large enough for both choices.

Mesons with very low energies will become non-strange pseudo-scalars by default. The parameters f_v and γ_s are thus 'corrected' for threshold effects and should reflect the dynamics of hadronization rather than the kinematics. This 'correction' should be viewed with caution, however, as it depends strongly on the distribution of meson energies in the model and includes no phase-space factors for the behavior just above threshold.

6.2 MODEL PREDICTIONS

N_{chg} The number of stable charged particles produced per event is a function of r and f_v with negligible dependence on γ_s. The dependence on f_v arises from the decay products of vector mesons. Charm and bottom decay multiplicities will also affect the measured number of charged particles. The model includes the measured decay multiplicities for charm and bottom decays. A measured value of $N_{chg} = 12.7 \pm 0.7$ from the TPC [1] experiment at 23 GeV is consistent with the unpublished value from this experiment.

N_{ρ^0} The number of ρ^0 per event is chiefly a function of f_v with a slight dependence on r. A simultaneous comparison of N_{ρ^0} and the number of charged particles N_{chg} allows an estimate of f_v and r.

For each of 25 pairs of r and f_v values 4000 Field-Feynman Monte Carlo events were generated without initial state radiation. The Monte Carlo points were then adjusted to reflect the estimates of charm and η' contributions from Chapter 5.† The strangeness suppression was set to $\gamma_s = 0.28$ ($r_s = 0.125$) and

† The Monte Carlo tends to overproduce η' and does not include any charm decays to ρ^0.

has little effect on f_v. The predicted average charged multiplicity, N_{chg}, and the number of ρ^0 with $p > 1$ GeV/c per event were compared with the measured rates. Figure 6.2 shows a comparison of N_{chg} vs N_ρ as a function of r and f_v with the data. The statistical error on the Monte Carlo points is around 0.02 for N_ρ and 0.05 for N_{chg}. The Monte Carlo points have been smoothed by a least squares fit to straight lines.The residual kinks in the lines are an artifact of the plotting procedure.

The plot indicates that $f_v = 0.37 \pm 0.07 \pm 0.09 \pm 0.10$, where the first error is the statistical error, the second is the systematic uncertainty in the measurement and the third reflects the uncertainties in the decay contributions. The best value of r is 1.1 ± 0.5 which corresponds to $M = 10.6 \pm 0.8$.

6.3 STRANGENESS SUPPRESSION

The same procedure can be used to determine γ_s from the measured number of K^0 per event. As each K^* decays to one K, the vector fraction should have no effect on the K^0 rate to first order. The vector fraction only enters in the variation of M needed to keep the charged multiplicity constant. As this variation is reasonably small, the vector fraction has little effect on the strangeness suppression. Figure 6.3 compares the Monte Carlo prediction for N_{K^0} for all p and N_{chg} with the data. The vector fraction was set to 0.5. The best value of γ_s is $0.30 \pm 0.02 \pm 0.07 \pm 0.05$ where the third error reflects the uncertainty in the charm branching fraction $B(c \rightarrow \bar{K}^0 + X) = 37 \pm 9\%$. If the charm fraction into K^0 is raised to 50%, the value of γ_s drops to 0.24.

Baryons Strange baryon production can alter the calculated relation between γ_s and the number of kaons per event. Strange quarks will either end up in kaons

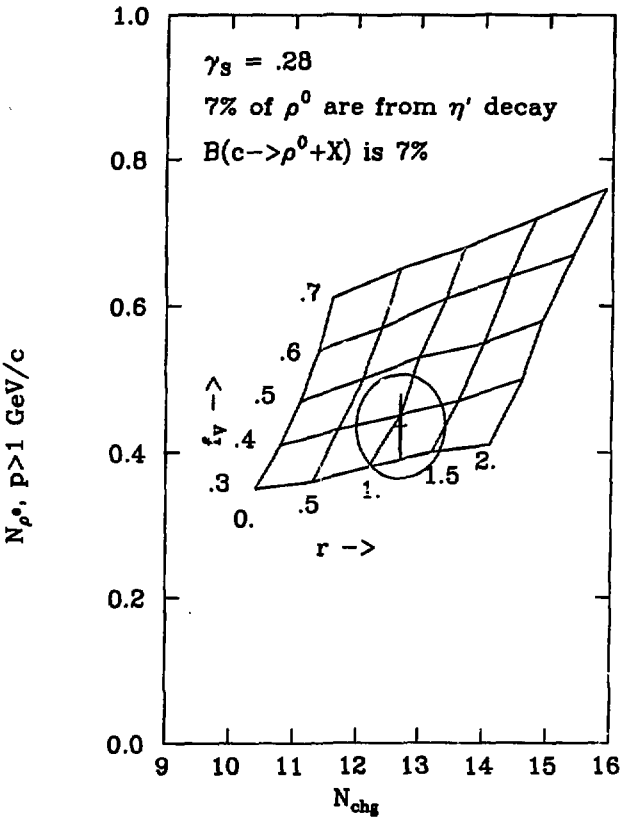

Figure 6.2: N_{ρ^0} with $p > 1$ GeV/c vs. N_{chg}. The grid represents the Monte Carlo predictions as a function of r and f_v. The errors on the data point are statistical only while the ellipse represents the total measurement uncertainty.

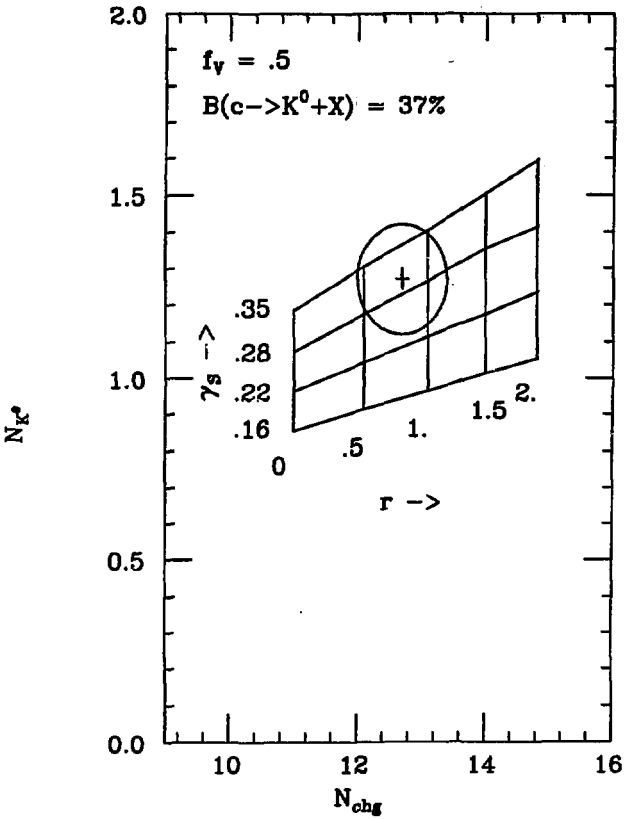

Figure 6.3: $N_{K^0+\bar{K}^0}$ vs. N_{ch_b} The Monte Carlo prediction has been adjusted to reflect the measured charm branching fractions.

or strange baryons. Thus, for a given γ_s, a high baryon rate will reduce the measured number of K^0. The Λ rate in the Monte Carlo is 0.25 consistent with the measured rate from this experiment of 0.22 ± 0.03. The bias due to baryon production should therefore be small.

LUND model The JADE collaboration [21] has also performed the same analysis with the LUND Monte Carlo [30]. If the measured values of N_{ch_g} and N_{K^0} from this experiment are interpreted with the JADE LUND model calculation, the value of γ_s is found to be $0.22 \pm 0.02 \pm 0.07$. This difference may be due to the unspecified charm branching fraction into K^0 in the LUND calculation. The LUND model does not use the measured charm branching fractions. Instead, a theoretical model of charm decay is used which may yield a higher K^0 branching fraction than the measured value.

As the K^0 rate includes the decay products of K^* the value of γ_s obtained above represents the average strangeness suppression for pseudo-scalar and vector particles. This average suppression is more pronounced than the 0.57 ± 0.20 found for vector particles alone in Chapter 5. The difference in strangeness suppression factors can be accounted for if the vector fraction parameter f_v is different for strange particles and non-strange particles. If strange mesons are more likely than non-strange mesons to be vectors, the number of K^* will be enhanced relative to ρ^0 thus decreasing the measured strangeness suppression in the vector meson sector. The measurements of the F_v^{ns} and F_v^s at the end of Chapter 5 indicate this as well.

The strange vector fraction parameter f_v^s can be evaluated by comparing the measured ratio of K^{*0} to K^0 with the Monte Carlo prediction for varying values of f_v. Only K^0 and $\overline{K}^{*0}$ with $p > 1$ GeV/c are included in the comparison.

Figure 6.4 shows the variation of K^*/K with f_v for r=1 and $\gamma_s = .28$. For the measured K^{*0} to K^0 ratio of $0.46 \pm 0.05 \pm 0.11$ the favored strange vector fraction parameter is $f_v^s = 0.70 \pm 0.08 \pm 0.16 \pm 0.08$ where the last error is from uncertainty in the charm contributions. (The parameter f_v measured from the ρ^0 rate includes only non-strange mesons and will be referred to as f_v^{ns} hereafter.)

6.4 SUMMARY OF FIELD-FEYNMAN PARAMETERS

Table 6.1 summarizes the Field Feynman parameters and compares them with the ratios measured in Chapter 5. As expected, the measured ratios are consistently smaller than the Field-Feynman parameters.

F-F parameter	measured ratio
$r = 1.1 \pm 0.5$	unknown
$M = 10.6 \pm 0.8$	10.9 ± 1.4
$f_v^{ns} = 0.37 \pm 0.07 \pm 0.13$	$F_v^{ns} = 0.30^{+0.17}_{-0.12}$
$f_v^s = 0.70 \pm 0.08 \pm 0.18$	$F_v^s = 0.57 \pm 0.20$
$\gamma_s = 0.30 \pm 0.02 \pm 0.09$	$R_s = 0.25 \pm 0.10$

Table 6.1: Comparison of Field-Feynman parameters and measured ratios. The errors are highly correlated as the same data is used for both analyses.

These results indicate that vector fractions are significantly different for strange and non-strange mesons. This is consistent with recent theoretical predictions[2, 3, 4, 5].

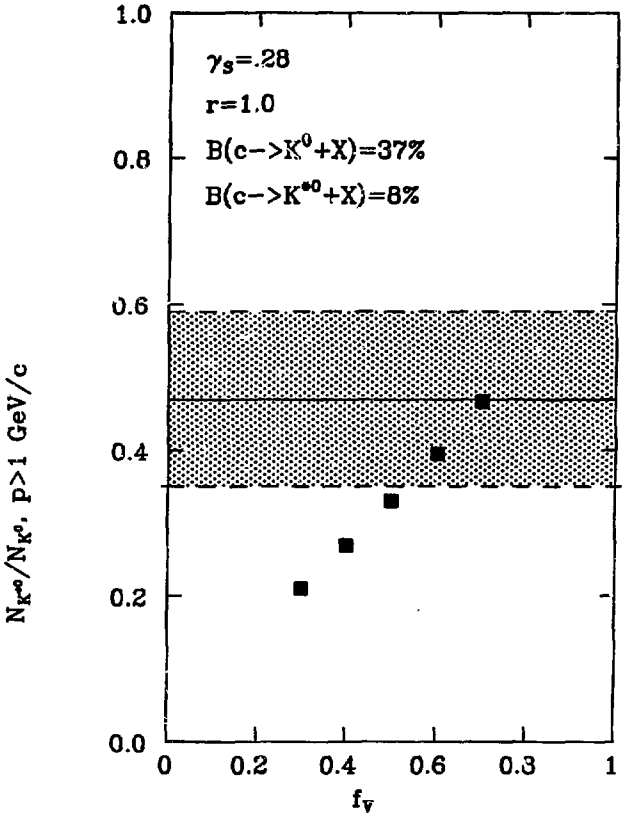

Figure 6.4: Ratio of K^{*0} to K^0 for $p > 1$ versus f_v. The shaded region denotes 1σ errors for the measured ratio.

6.5 STRING MODELS

The LUND model [2, 31] is a fragmentation model based on 1-dimensional color strings. The color flux between the initial colored partons is assumed to form a narrow string-like structure with a constant tension per unit length. As the partons separate, the energy in the string increases until the formation of $q\bar{q}$ pairs along the string is favored energetically. These $q\bar{q}$ pairs are created via quantum mechanical tunnelling. The tunnelling probability is presumed to be a function of the $q\bar{q}$ pair mass, the final state meson masses and the spin configuration of the quarks.

Particle production in the string model depends on the overlap of the string and particle wave functions. The production amplitude is assumed to be dominated by the normalization of the particle wave function near its center. The spin-spin interaction is repulsive for the triplet states and spreads the wave function over a wider region of space. The binding energy is correspondingly reduced, leading to a higher mass. Due to the repulsion, the amplitude of the wave function near the origin is reduced and is believed to scale as $1/m^{\frac{1}{2}}$, where m is the meson mass. The production probability thus scales as $1/m$. These predictions are described in reference 2.

The model predicts that the ratio of pseudo-scalar to vector mesons scales as the ratio of the masses M_v/M_{ps}. For values of the mass ratio near unity the ratio of pseudo-scalars to vectors is predicted to be $1/3(M_v/M_{ps})$; for equal masses this yields the familiar 1:3 derived from spin counting. For values of the mass ratio greater than 5, the pseudo-scalar to vector ratio is predicted to reach a plateau at a value of 2.8. These predictions are for the vector and strange fractions after kinematic effects such as mass thresholds have been removed and

should thus be compared with 'corrected' parameters such as those obtained from the Field-Feynman model rather than the raw ratios from Chapter 5. Table 6.2 summarizes the results from this experiment and Figure 6.5 shows the ratios from this experiment compared with results from other experiments. The JADE and TASSO results are derived from a fit to LUND[30] model parameters analogous to f_v^s and f_v^{ss}. The results from this experiment agree quite well with the string model prediction.

	mass ratio	PS/V	reference
non-strange	5.5	$1.7 \pm 0.5 \pm 0.7$	
strange	1.8	$0.4 \pm 0.2 \pm 0.4$	
Charm (D^*/D)	1.0	0.3 ± 0.5	HRS[26]

Table 6.2: Comparison of PS:V ratios with mass ratios

This model also predicts that the production of strange quarks in hadronization will be suppressed by a factor $e^{-\pi\mu^2/\kappa}$, where μ is the strange quark mass and κ is the string tension, of order 0.2 GeV^2. For u and d quark masses of 100 MeV/c^2 and an s quark mass of 300 MeV/c^2, the s quark suppression factor will be 0.28, in good agreement with the Field-Feynman parameter $\gamma_s = 0.30 \pm 0.09$ and the measured ratio $R_s = 0.25 \pm 0.10$.

The LUND string model thus agrees with the observed behavior of the relative suppressions of both vector and strange mesons. It should be noted, however, that the 'correction' for kinematic effects from the Field-Feynman model is quite crude and could have a significant effect on the results.

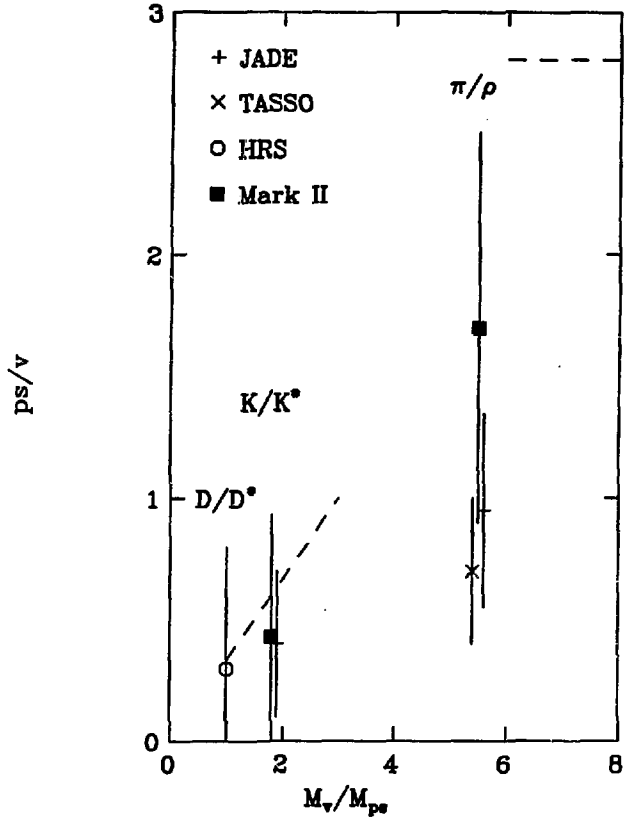

Figure 6.5: Pseudo-scalar to vector ratio as a function of mass ratio. The dashed lines represents the theoretical prediction for small and large values of M_v. The TASSO point is from reference 16, the JADE points are from reference 21 and the HRS point is from reference 26.

6.6 CLUSTER MODELS

In QCD cluster models [3, 4, 5] the initial partons in the event are evolved by leading-log QCD (Figure 1.1 illustrates the evolution of an event in this model) to produce a shower of partons. The partons are then combined into color singlet clusters with masses of order 1 GeV. These clusters decay into the final state particles via phase space with appropriate spin factors. No explicit strange particle or baryon suppression is included in the model. The measured rates for hadrons are thus determined solely by spin statistics, phase space and the typical cluster mass.†

As the relative rates for meson production are determined at the cluster level, qualitative predictions can be derived from 2-body phase space decays of single clusters. A simple phase space model can be constructed in which a quark of flavor u, d, or s and an anti-quark of independent flavor u, d or s are chosen to form a cluster. The cluster is assigned a mass M and then decayed by phase space to 2 mesons (Figure 6.6). The final state mesons are chosen to be pseudo-scalars or vectors for convenience and the final states are weighted by the phase space factor $2q/M$ (where q is the center of mass momentum of the mesons and M is the cluster mass) and by final state spin factors. No explicit suppression of strange mesons is included. All possible combinations of quarks and spins are included to produce phase-space weighted production rates for mesons. As these mesons are not decayed, the rates are for 'primary' mesons.

† As the measured rates are *determined* by phase space and mass thresholds, the 'corrected' vector and strangeness suppressions defined in the Lund and Feynman-Field have no meaning in this model.

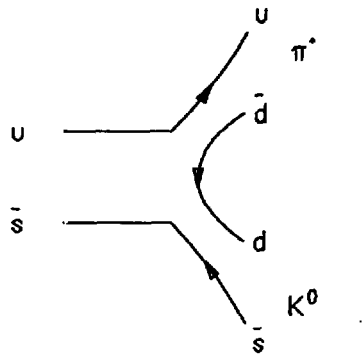

Figure 6.6: Two-body decay of a cluster

Figure 6.7 shows the fractions of all primary light mesons which are $\pi^{\pm}$, K^0, ρ^0 or K^{*0} as a function of the cluster mass M. The wiggles in the fractions are due to thresholds for competing particles. The non-strange pseudo-scalars are favored at low cluster masses. In the large mass limit, the vector meson rates are 3 times as high as the pseudo-scalar rates and no strangeness suppression remains.

Real events will have a spectrum of cluster masses. Figure 6.8 shows the distribution of mesons for clusters made with probability $P(M) = e^{-M/M_0}$ as

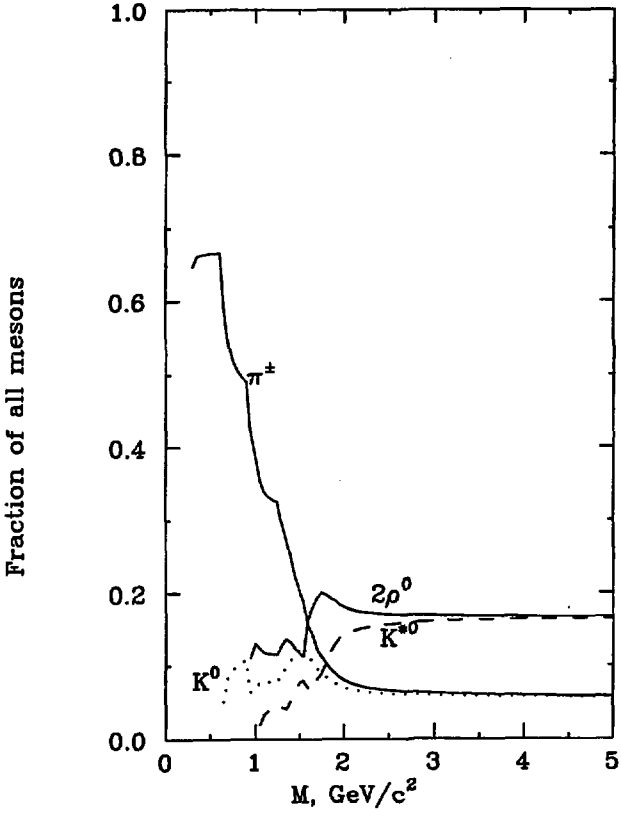

Figure 6.7: Meson fractions as a function of the cluster mass, M.

a function of M_0. Figures 6.9a and b show the strange and non-strange vector fractions, F_v^s and F_v^{ns}, as a function of M_0 and Figure 6.9c shows the strangeness suppression, R_s, for all mesons.

For mass scales $M_0 \sim 1.5$ GeV/c^2, this phase space model is compatible with the observed ratios. Studies of different cluster mass distribution functions indicate that only those distributions which have a large proportion of the clusters in the range $0.3 - 1.0$ GeV/c^2 reproduce the data.

This model is a gross simplification of the actual processes which give rise to mesons. It includes only pseudo-scalar and vector mesons and only 2-body decays. It does serve as a demonstration that simple kinematics can have a pronounced effect on the relative production rates for particle species of differing masses.

6.7 CONCLUSION

The inclusive production rates for K^0, K^{*0} and ρ^0 have been measured and compared with the Lund string model and a simple phase space model. Both models reproduce the measured differences between the production rates of strange and vector mesons.

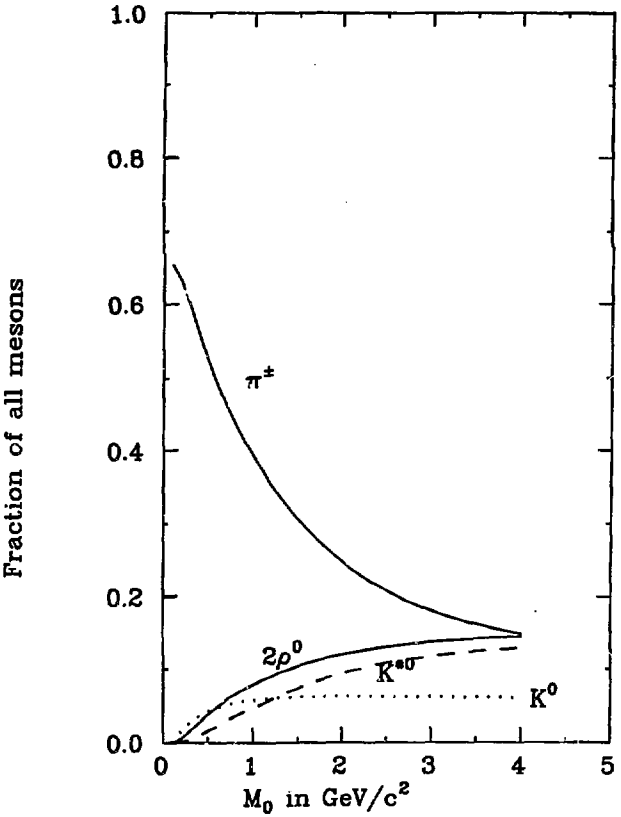

Figure 6.8: Meson fractions as a function of the typical mass, M_0, where $P(M) = e^{-M/M_0}$.

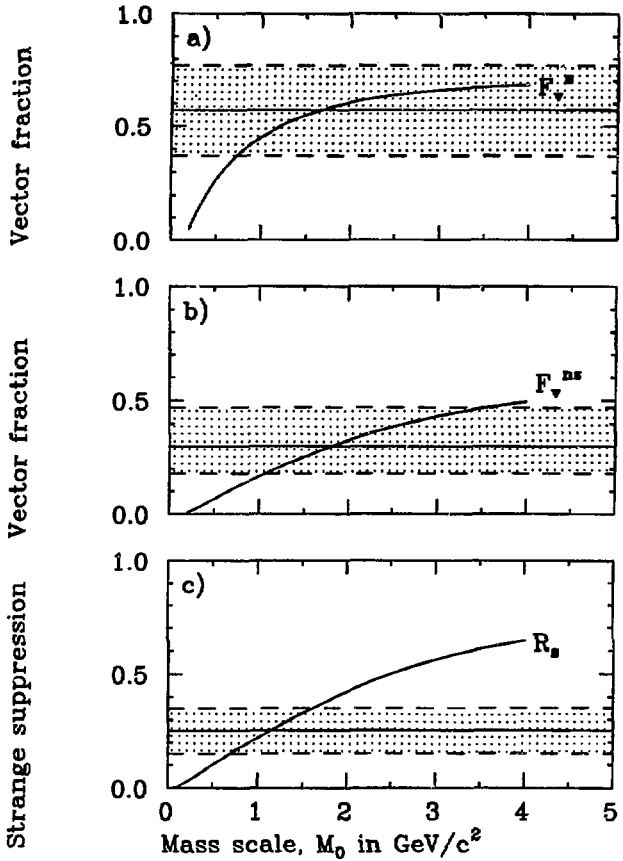

Figure 6.9: a) and b) Vector fractions for strange and non-strange mesons. c) Strangeness suppression R_s for all mesons. $P(M) = e^{-M/M_0}$ as before. The shaded areas represent 1 σ errors for the measured ratios.

References

1. H. Aihara *et.al.*, Phys. Rev. Lett. 52, 577 (1984)
2. B. Andersson *et.al.*, Phys. Rep. 97, 31 (1983)
3. T. Gottschalk, Nucl. Phys. B239,325 (1984)
4. R. Field and G. Fox, Cal. Tech. note CALT-68-965 (1982)
5. G. Marchesini and B. Webber, Nucl. Phys. B238, 1 (1984), B. Webber, Nucl. Phys. B238, 492 (1984)
6. R. Schindler *et.al.*, Phys. Rev. D24, 78 (1981)
7. J. Jaros in Proceedings of the International Conference on Instrumentation for Colliding Beam Physics, SLAC-Report 250, edited by W. Ash, Stanford CA, 29 (1982)
8. W. Davies-White *et.al.*, Nucl. Instr. and Meth. 160, 227 (1979)
9. J. Patrick *et.al.*, Phys. Rev. Lett. 49, 1229 (1982)
10. M. Levi *et.al.*, Phys. Rev. Lett. 51, 1941 (1983)
11. A. Ali *et.al.*, Phys. Lett. 93B, 155 (1980)
12. R. Field and R. Feynman, Nucl. Phys. B136, 1 (1978)
13. G. Bonneau and F. Martin, Nucl. Phys. B27,381 (1971)
14. F.A. Berends and R. Kleiss, Nucl. Phys. B177, 141 (1981)
15. T. Himel, SLAC PUB 223 (1979) (unpublished)
16. R. Brandelik *et.al.*, Phys. Lett. 117B 135 (1982)
17. W. Bartel *et.al.*, DESY 84-058 (1984)
18. J. Dillon, VFINDP Vee finder, Trilling-Goldhaber Group Physics note #232, March 1982
19. R. Brandelik *et.al.*, Phys. Lett. 94B, 91 (1980)

20. Ch. Berger *et.al.*, Phys. Lett. 104B, 79 (1981)

21. W. Bartel *et.al.*, Z. Phys. C 20, 187 (1983)

22. H. Aihara *et.al.*, LBL-18325 (Sept. 84)

23. M. Althoff *et.al.*, Z. Phys. C 17, 4 (1983)

24. Aguilar-Benitez *et.al.*, Rev. Mod. Phys. 56, No. 2, Part II (1984)

25. D. Hitlin, talk delivered at SLAC Summer School, 1984 (unpublished)

26. S. Ahlen *et.al.*, Phys. Rev. Lett. 51, 1147 (1983)

27. W. Bartel *et.al.*, Phys. Lett. 130B, 454 (1983)

28. H. Aihara *et.al.*, Phys. Rev. Lett. 52, 2201 (1984)

29. M. Althoff *et.al.*, Phys. Lett. 130B, 340 (1983)

30. B. Andersson and G. Gustafson, Z. Phys C3, 223 (1980), T. Sjöstrand, Computer Phys. Comm. 27, 243 (1982)

31. B. Andersson *et.al.*, Z. Phys. C20, 317 (1983)

This report was done with support from the Department of Energy. Any conclusions or opinions expressed in this report represent solely those of the author(s) and not necessarily those of The Regents of the University of California, the Lawrence Berkeley Laboratory or the Department of Energy.

Reference to a company or product name does not imply approval or recommendation of the product by the University of California or the U.S. Department of Energy to the exclusion of others that may be suitable.